

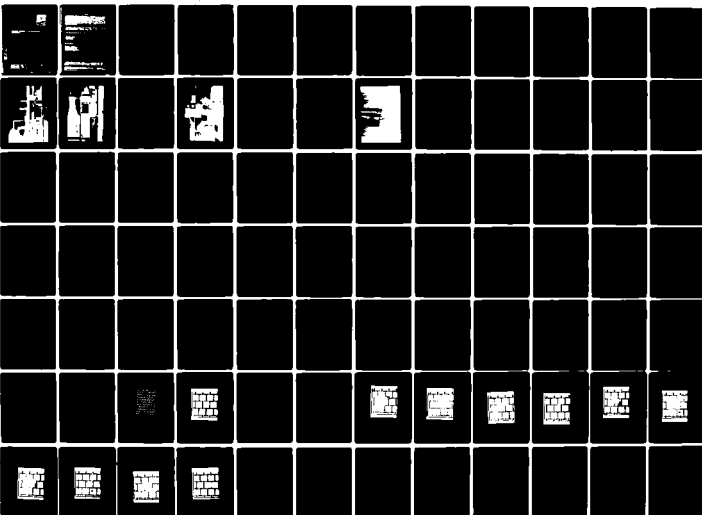
**F/8 9/2**

**F33615-77-C-1002**

100.  
NI

1 of 2

20.  $A)BC \times 9C$



UNCLASSIFIED

SECURITY CLASSIFICATION OF THIS PAGE (When Data Entered)

19 REPORT DOCUMENTATION PAGE		READ INSTRUCTIONS BEFORE COMPLETING FORM
1. REPORT NUMBER 18 AFAL-TR-79-1145	2. GOVT ACCESSION NO.	3. RECIPIENT'S CATALOG NUMBER
4. TITLE (and Subtitle) 4 EPITAXIAL MAGNETIC FILM EVALUATION TECHNIQUES	5. TYPE OF REPORT & PERIOD COVERED Interim 11/1/77-10/31/78	
7. AUTHOR(s) 10 Philip E. Wigen and Kenneth J. Breeding	6. PERFORMING ORG. REPORT NUMBER 764596/710525	
9. PERFORMING ORGANIZATION NAME AND ADDRESS The Ohio State University Research Foundation, 1314 Kinnear Road Columbus, Ohio 43212	8. CONTRACT OR GRANT NUMBER(s) Contract No. F33615-77-C-1002	
11. CONTROLLING OFFICE NAME AND ADDRESS AFAL/DHR WPAFB, Ohio 45433	10. PROGRAM ELEMENT, PROJECT, TASK AREA & WORK UNIT NUMBERS 10 2305 R1-70 (1) R1	
13. MONITORING AGENCY NAME & ADDRESS (if different from Controlling Office) 9 Interim rept. 1 Nov 77 - 31 Oct 78	12. REPORT DATE 11 November 1979	
16. DISTRIBUTION STATEMENT (of this Report) "Approved for public release; distribution unlimited." 14 OSUPF-764-96/710525	13. NUMBER OF PAGES 110 PP. 11 B	
17. DISTRIBUTION STATEMENT (of this Report)	15. SECURITY CLASS. (of this Report) Unclassified	
18. SUPPLEMENTARY NOTES	15a. DECLASSIFICATION/DOWNGRADING SCHEDULE	
19. KEY WORDS (Continue on reverse side if necessary and identify by block number) magnetic bubble materials      microscopic positioning M-H looper      integrated optics Domain walls optical scanning		
20. ABSTRACT (Continue on reverse side if necessary and identify by block number) This annual report reviews the progress of the second year of work on magnetic bubble materials and the testing of bubble memory devices. At the Avionics Laboratory, an M-H looper device was built for use in characterizing bubble materials. The device is fully automated (employing a Hewlett-Packard calculator system) and for use with whole wafers of bubble material. Details of the looper along with samples of data taken are included in the report. At the OSU Physics department, two types of domain wall phenomena were investigated. Propagation of spin waves through domain walls at microwave		

DD FORM 1473  
1 JAN 73

UNCLASSIFIED

SECURITY CLASSIFICATION OF THIS PAGE (When Data Entered)

267 366

JTB

Unclassified

SECURITY CLASSIFICATION OF THIS PAGE(When Data Entered)

Block #20 (Abstract) -- Continued

frequencies were investigated both theoretically and experimentally. Secondly, domain wall motion excited with a radio frequency magnetic field oriented parallel to the film plane was studied.

Three studies related to the testing of large scale bubble memories were undertaken. In the first, a technique was developed which optically scanned a bubble memory overlay pattern to identify and locate faults in the pattern. Some preliminary experiments indicate the feasibility of this approach. The second study looked into the microscopic positioning of the bubble memory chip. It was found that the positioning mechanism can be consistent with accuracies of  $0.5\mu\text{m}$ . Thus  $1\mu\text{m}$  element overlay patterns can be scanned as indicated above. Finally an integrated optics approach was examined for application to dynamic testing. Although much work remains to be done, it appears that the approach described here is possible.

SECURITY CLASSIFICATION OF THIS PAGE(When Data Entered)

## PREFACE

This technical report covers the research performed under Contract No. F33615-77-C-1002 from 1 November 1977 to 31 October 1978. The previous interim report is #AFAL-TR-78-67.

The contract is with the Physics Department with Professor P. E. Wigen as co-principal investigator and the Electrical Engineering Department with Professor K. J. Breeding as co-principal investigator. Both departments are located at The Ohio State University. The thrust of the work was Epitaxial Magnetic Film Evaluation Techniques, and is conducted under the direction of Dr. Millard Mier, AFAL/DHR, Avionics Laboratory, Wright-Patterson Air Force Base, Ohio.

J. P. Omaggio and M. P. Globe were involved in this program at the Avionics Laboratory, A. A. Parker and P. Lemaye were involved in this program at the Physics Department, OSU and H. K. Brown and R. Thienlikit were involved in this program at the Electrical Engineering Department, OSU.

## TABLE OF CONTENTS

SECTION	PAGE
I. MATERIALS RESEARCH . . . . .	1
A. M-H Looper . . . . .	1
1. Introduction . . . . .	1
2. Principle of Operation . . . . .	3
3. Conclusions and Final Comments . . . . .	15
B. Spin Wave Excitations in Domain Walls . . . . .	18
C. Radio Frequency Domain Wall Oscillations . . . . .	38
II. TESTING PROGRAM . . . . .	59
A. Overlay Pattern Verification . . . . .	59
B. Positioning Problem. . . . .	79
C. Optical Waveguide . . . . .	84
D. References . . . . .	87
APPENDIX A. Helmholtz Coils . . . . .	90
B. Signal Processing Program for the M-H Looper . . . . .	95
C. Program to calculate stripe period as a function of Bias Field . . . . .	98
D. Curve Fitting Program for FMR Data . . . . .	100

A

# LIST OF ILLUSTRATIONS

FIGURE	PAGE
1 Block diagram of M-H looper.	4
2 The M-H looper. Shown are the frequency generator, the bipolar power supply, the sense resistor box, the capacitor bank and the drive coil assembly.	5
3 The M-H looper. Shown are the electronics and compensation bridge box, the oscilloscope and the calculator controlled voltmeter. The sample wafer (top) and sense resistor signals can be seen on the oscilloscope.	6
4 A close up view of the X-Y translation device and the drive coils.	8
5 A close up view showing the placement of the sample and compensation coils and the sample wafer.	11
6 An M-H trace for an 8.3 $\mu$ m thick bubble film.	13
7 A typical dM/dH vs. H trace from the M-H Looper.	14
8 Coordinate system used in the derivation of equation of motion. The domain wall is in the XZ plane. X is the film normal.	19
9 $\theta$ as a function of the reduced variable $\eta$ .	21
10 The effective potential $-2\text{sech}^2\eta$ as a function of $\eta$ the dimensionless length variable.	24
11 Symmetric part of the spin-wave solution to Eq. (16).	26
12 Solid line: Integral of the low field signal after subtracting the base line due to the uniform mode. Dotted line: The inverse stripe period scaled to match the solid line at zero field.	33
13 The reduced intensity ratio $R_0/(1+k^2)$ as a function of the wave vector k. The solid line shows the theoretical calculations. The data points are shown by astericks. Data was taken at 9.2 GHz. Best fit was obtained for $a=0.3 P_0$ .	

# LIST OF ILLUSTRATIONS (cont)

FIGURE		PAGE
14	Signal Strength and S/N as a function of RF power.	39
15	Signal Strength and S/N as a function of Bridge isolation.	40
16	Typical direct absorption spectrum.	41
17	Bridge isolation vs. frequency-resonator type spectrometer. Spectrometer will only operate when isolation is -5dB or greater.	42
18	Diagram of a short section of helical transmission line.	44
19	Frequency response of helical transmission line.	45
20	Frequency Response-Spectrometer with helical transmission line and matching network.	46
21	Fixed coordinate system xyz.	48
22	Numerical solution for domain wall position as a function of time. Closed line shows time dependence of inplane RF magnetic field to show the phase relationship between drive field and wall motion.	51
23	Power absorption in frequency sample 3-18-16.	56
24	Power absorption vs. frequency sample TI 330. Theory curve is least squared fit to data points.	57
25	Original Overlay Pattern.	63
26	Control Image.	64
27	Large Additive Fault.	67
28	Small Additive Fault.	68
29	Large Subtractive Fault.	69
30	Small Subtractive Fault.	70
31	Large Additive Fault, T=6.	71
32	Small Additive Fault, T=6.	72
33	Large Subtractive Fault, T=6.	73.
34	Small Subtractive Fault, T=6.	74

LIST OF ILLUSTRATIONS (cont)

FIGURE		PAGE
35	Large Additive Fault, $T=6$ .	75
36	Small Additive Fault, $T=2$ .	76
37	Large Subtractive Fault, $T=2$ .	77
38	Small Subtractive Fault, $l=2$ .	78



## LIST OF TABLES

TABLE	PAGE
1. Drive coils: DC Characteristics . . . . .	10
2. Comparison of VSM and M-H Looper Measurements for $\chi_o$ . .	16
3. Material Parameters. . . . .	35
4. Experimental Results . . . . .	36
5. Material Parameters of Sample 3-18-16 . . . . .	50

## SECTION I

### Materials Research

#### A. M-H Looper

##### 1. Introduction

The characterization of the static parameters of a magnetic bubble material traditionally consists of three parameters. The film thickness  $h$ , the stripewidth  $w$ , at zero applied field and the bubble collapse field  $H_{bc}$  are measured<sup>(1)</sup>. All pertinent static parameters can be calculated from these three terms. These include the saturation magnetization, the domain wall energy density, the material characteristic length and others. Ordinarily, the stripewidth and collapse field measurements are done optically with a microscope. As bubble sizes decrease, the difficulties in these measurements increase.

A determination of the hysteresis loop of a wafer provides an alternative to optical measurements. Measurement of the initial susceptibility,  $\chi_0 \equiv (dM/dH)_{m=0}$  and stripe collapse field,  $H_{sc}$  from the hysteresis loop are substituted for  $w$  and  $H_{bc}$ .

From the stripe domain stability conditions developed by Kooy and Enz<sup>(2)</sup> the relationship between the film magnetization and the applied magnetic field is given as:

$$\frac{4\pi M - H}{4\pi M_s} + \frac{2\sqrt{\mu}}{1 + \sqrt{\mu}} - \frac{1}{\pi^2 \alpha} \sum_{n=1}^{\infty} \frac{1}{n^2} \sin(\pi n(1 + \frac{M}{M_s})) [1 - \exp(-2\pi n \alpha)] = 0. \quad (1)$$

$M$  is the net magnetization of the film,  $M_s$  is the saturation magnetization,  $H$  is the applied field,  $n$  is the film thickness,  $\mu \equiv 1 + 2\pi M_s^2 / K_u$ ,  $\alpha \equiv h\sqrt{\mu} / (d_1 + d_2)$ ,  $d_1$  is the stripe width for domains with  $\vec{M}$  in the direction of  $\vec{H}$  and  $d_2$  is for domains with  $\vec{M}$  in the opposite direction. The equation assumes a film of infinite area with straight domains.

The domain wall energy can be related to the magnetization by the equation:

$$\frac{\sigma_w}{(4M_s)^2 h \sqrt{\mu}} \left( \frac{1 + \sqrt{\mu}}{2\sqrt{\mu}} \right) = \frac{1}{4\pi^2 \alpha^2} \sum_{n=1}^{\infty} \frac{1}{n^3} \sin^2 \left[ \frac{n\pi}{2} \left( 1 - \frac{M}{M_s} \right) \right] [1 - (1 + 2\pi n \alpha) \exp(-2\pi n \alpha)] \quad (2)$$

In this equation,  $\sigma_w$  is the energy of the domain wall per unit area.

If the uniaxial anisotropy field is large compared to  $4\pi M_s$  and  $\mu \gg 1$ , the above equations reduce to<sup>3</sup>:

$$\frac{4-M-H}{4-M_s} + \frac{d}{\pi^2 h} \sum_{n=1}^{\infty} \frac{1}{n^2} \sin[n\pi(1 + \frac{M}{M_s})] [1 - \exp(\frac{-2\pi n h}{d})] = 0 \quad (3)$$

and

$$\frac{\lambda}{h} = \frac{d^2}{\pi^3 h^2} \sum_{n=1}^{\infty} \frac{1}{n^3} \sin^2 \left[ \left( \frac{n\pi}{2} \right) \left( 1 - \frac{M}{M_s} \right) \right] [1 - \exp(\frac{-2\pi n h}{d})] \left( 1 + \frac{2\pi n h}{d} \right) \quad (4)$$

where  $d = d_1 + d_2$  and  $\lambda$  is the material length ( $\equiv \sigma_w / 4\pi M_s^2$ ).

From equation 3 the initial susceptibility is calculated.

$$4\pi\chi_0 = \left[ 1 + \frac{2w}{\pi h} \sum_{n=1}^{\infty} \frac{1}{n} (-1)^n [1 - \exp(\frac{-\pi n h}{w})] \right]^{-1} \quad (5)$$

where  $w \equiv d/2$ . The relation between  $\chi_0$  and  $w/h$  can be graphed or tabulated and if  $\chi_0$  is measured,  $w/h$  can be determined<sup>(3)</sup>. Similarly, using equation 4,  $\chi_0$  and  $\lambda/h$  can be related. Using Thiele's conditions for

bubble stability<sup>(4)</sup>, graphs of  $4\pi M_s$  against stripe collapse field can be drawn. If an independent measurement of  $h$  is made,  $w$  and  $4\pi M_s$  are determined.

## 2. Principle of Operation

The principle of operation of the hysteresis loop device ("M-H Looper") is to place a sample in an alternating magnetic drive field ( $H_d = H_0 \sin \omega t$ ) and by using a small pick up coil placed in close proximity to the sample, measure the sample's magnetization as a function of applied field. Figure 1 is a block diagram of the system including sample positioning and pick up coil placement.

Since the change in the magnetic flux linkage through the sample pick up coil will be dominated by the changes in  $H_d$  rather than the change in the sample magnetization, a second "compensation" pick up coil is required. This second coil is placed in a location such that the changes in  $H_d$  can be monitored while the change in the sample magnetization will have a negligible effect on the induced voltages in this coil.

The signal from the compensation coil,  $V_{comp}(t)$ , is amplified and subtracted from the amplified sample coil signal,  $V_{samp}(t)$ , such that  $V_{sig} = V_{samp} - V_{comp} = 0$  when no sample is present. Thus, when a sample is present,  $V_{sig}(t)$  is directly proportional to the time derivative of the sample magnetization, i.e.  $V_{sig} \propto dM(t)/dt$ . Signal processing and hysteresis loop display are fully automated using a desk top calculator system. Figures 2 and 3 are photographs of the system. The desk top calculator and plotter are not shown.

### a. Drive System

For operation of the looper, rapidly varying (for reasonable signal strength) homogeneous fields of sufficient intensity to

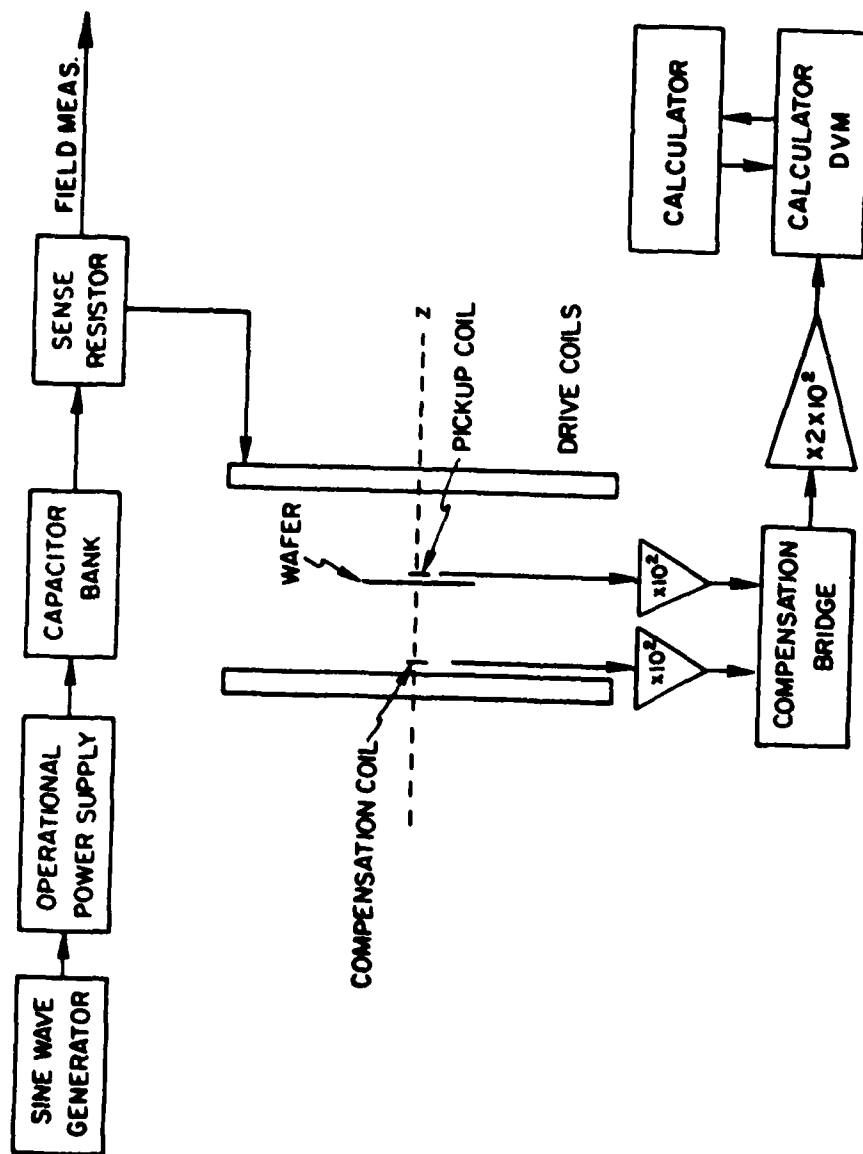


Figure 1. Block diagram of M-H 100per.

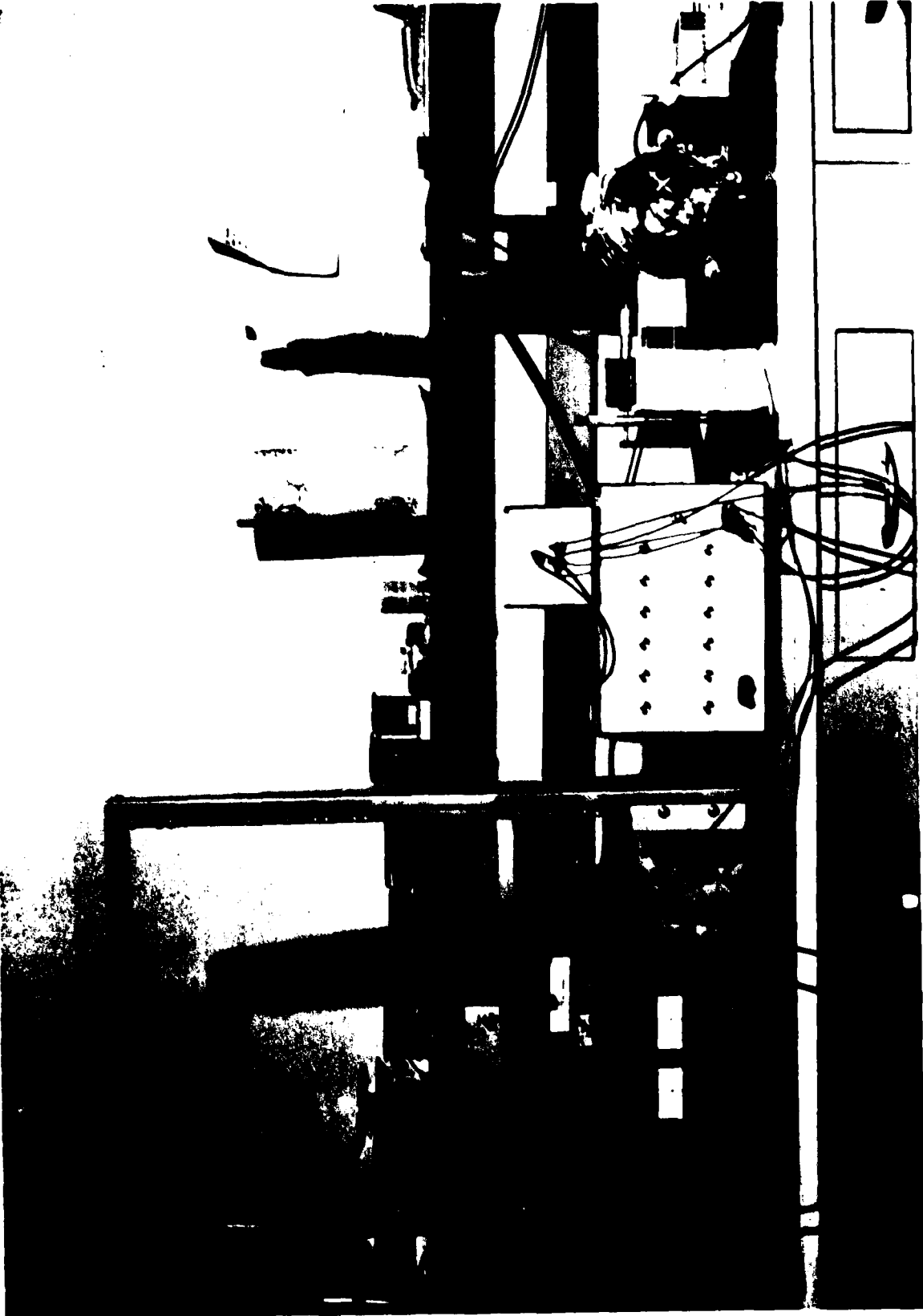


Figure 2. The M-H looper. Shown are the frequency generator, the bipolar power supply, the sense resistor box, the capacitor bank and the drive coil assembly.

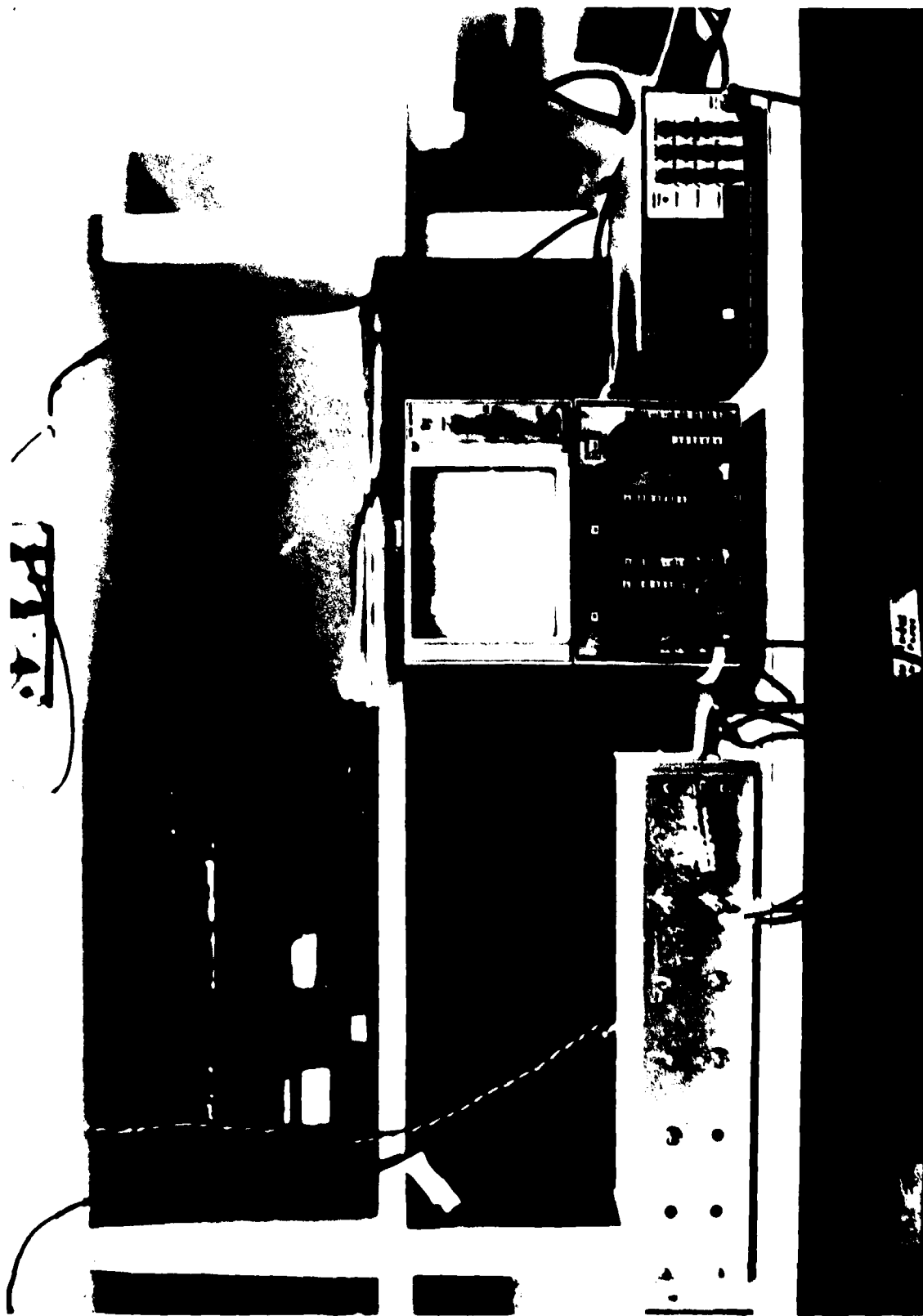


Figure 3. The W-H looper. Shown are the electronics and compensation bridge box, the oscilloscope and the calculator controlled voltmeter. The sample water (top) and sense resistor signals can be seen on the oscilloscope.

saturate bubble materials are desired. These fields are produced with a set of Helmholtz coils driven by a Kepco 15-20 M bipolar operational power supply. The coils have 300 turns of #14 gauge copper wire and are potted with stycast #1266 heat conducting epoxy to help eliminate vibration within the windings. Further design considerations are included in Appendix A. Figure 4 shows a close up photograph of the drive coils.

In the actual installation, the drive coils form a part of a tuned, series, RLC circuit. The impedance of this circuit is given by:

$$|Z| = \{R^2 + (\omega L - (\omega C)^{-1})^2\}^{1/2} \quad (6)$$

In this equation  $\omega$  is the radial frequency of the drive field,  $L$  is the inductance of the coils,  $R$  is the dc resistance of the coils and sense resistor and  $C$  is the capacitance of the tuning capacitor. In order to facilitate tuning and to allow for operation over a range of frequencies, a capacitance bank consisting of switch selectable parallel capacitors has been constructed. The maximum capacitance available is 110  $\mu$ f which allows a minimum impedance operation at frequencies as low as  $\sim 200$  Hz.

The current through the coils and thus the ac magnetic field is monitored by the ac voltage drop across a 75 W, .033  $\Omega$ , "non-inductive" resistor. The inductance of the sense resistor is small but not zero. However, at constant frequency, the inductive component of the impedance is constant and the potential across the sense resistor is proportional to field strength.

The sense resistor potential to field strength calibration was calculated by monitoring the induced emf (due to the drive field only) in the sample pick up coil. Knowing the drive field frequency and effective area of the coil, the sinusoidal field amplitude can be related to the emf amplitude.





Figure 4. A close up view of the  $V-V$  translator device and the drive coils.

The dc characteristics of the drive coils are given in Table I. The field strength was measured with a Hall effect gaussmeter. The field homogeneity was measured to be better than 1% across the surface of a 1" diameter wafer located at the central plane of the coils.

#### b. Sample Mounting and Pick up Coils

The sample mounting system was designed for use with 1" diameter wafers. This unit, constructed from teflon, has a 1" diameter recess in which the sample is firmly held. The holder is mounted on a precision X-Y translation stage which allows accurate and easy sample positioning. This holder can easily be modified to hold samples of arbitrary diameter.

The pick up coils have an outside diameter of .256" and were wound with #34 gauge copper wire on delrin forms. Both coils are mounted on the drive coil axis with the sample coil resting on the sample. The compensation coil is situated at the inner edge of one of the drive coils.

Details of the pickup coil placement are shown in Figure 5. A wafer in the sample holder mounted between the drive coils are also shown in Figure 5. The X-Y translation device is shown in Figure 4.

#### c. Signal Processing

In order to null out the background signal due to  $H_d(t)$ , a multi-arm compensation bridge was constructed. This bridge originally designed by Huber<sup>(5)</sup> for use in M-H loopers, has several branches which can be adjusted to eliminate the fundamental and higher harmonic signals from the pick up coils.

TABLE 1  
DRIVE COILS: DC CHARACTERISTICS

I (Amps)	H (oe.)	System Resistance (Coils in Parallel)
1	26.1	R = .7 $\Omega$
2	51.3	
5	123	
8	196	
10	243	
12	291	
14	338	
16	386	
18	434	
20	484	



Figure 5. A close up view showing the placement of the sample and compensation coils and the sample wafer.

Operational amplifiers amplify the sample and compensation coil signals ( $\times 10^2$ ) before entering the bridge circuit and the output of the bridge ( $\times 10^2$ ) before entering the calculator system.

Signal processing is accomplished using a Hewlett-Packard Model 9825A calculator system. Signal input is through a calculator controlled HP 3437A system voltmeter and plotting is on an HP 9872A plotter. The signal is portioned into a 500 channel array and signal averaging is achieved by sampling each channel 20 times. Final nulling of the drive field signal is achieved by sampling with a wafer in place and without, and then subtracting arrays. The array is numerically integrated with respect to time and plotted against  $H_d$ .

An M-H trace for an 8.3  $\mu\text{m}$  thick bubble material is shown in Figure 6. Traces of  $dM/dH$  vs.  $H$  are also available and an example of this is shown in Figure 7. A listing of the program used is in Appendix B.

#### d. Calibration

The field emanated from the sample,  $H_s$ , is detected in the pick up coil. Generally in hysteresis loop devices this field is proportional to some fraction of the sample moment  $m$ , or  $H_s = Km$ . In a vibrating sample magnetometer, VSM, the distance from sample to detection coils is large compared to the sample dimensions. For this reason the constant  $K$  has the same value for both film and substrate. A known change in moment of the paramagnetic substrate can be used to calibrate the moment axis of the hysteresis loop.

Unfortunately, in the M-H loopers this is not the case. The sample pick up coil rests on the film and the film to coil and substrate to coil distances (at least for a portion of the substrate) are significantly different. The constants  $K_f$  and  $K_s$  are different and a change in moment in the substrate (per unit time) will cause a potential in the pick up coil unlike that caused by the same change in moment in the film.

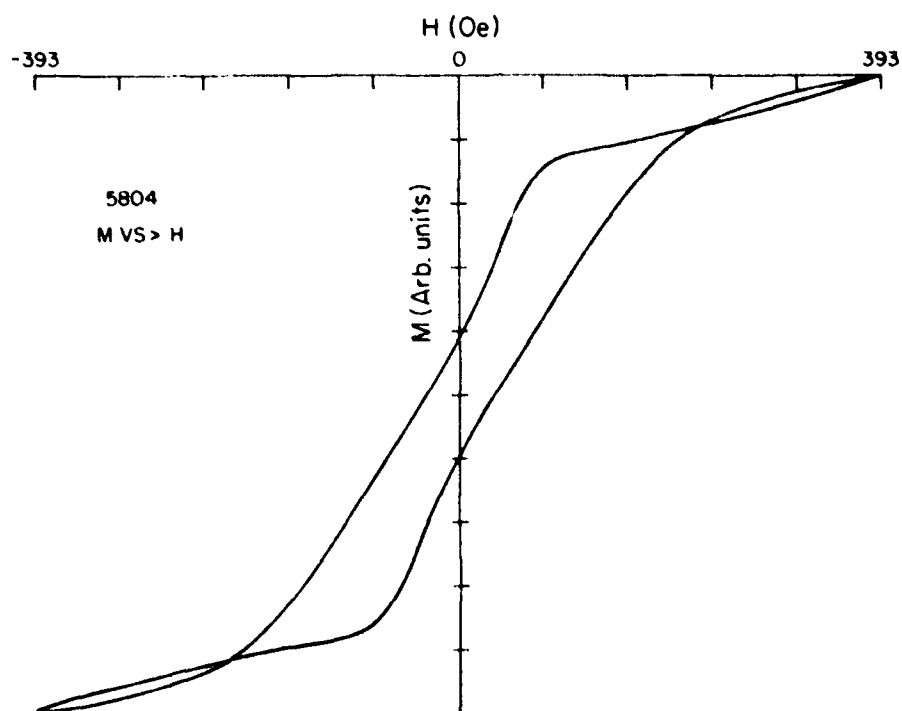


Fig. 6 An M-H trace for an  $8.3\mu\text{m}$  thick bubble film.

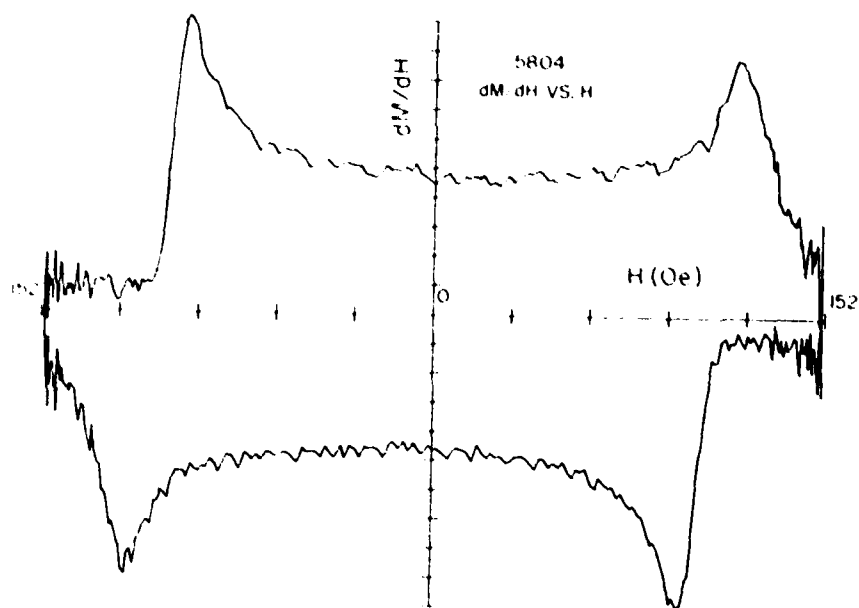


Fig. 7 A typical  $dM/dH$  vs.  $H$  trace from the M-H loop.

It can be seen from the above discussion that the gadolinium gallium garnet substrate cannot be used for calibration in the M-H loop. The use of a known or standard sample is substituted. The zero magnetization susceptibility of this sample is measured using a VSM.

With the use of a standard (an 8.3  $\mu\text{m}$  thick bubble wafer) the zero magnetization susceptibility of a 5.19  $\mu\text{m}$  and a 5.6  $\mu\text{m}$  wafer were measured. As a check  $\chi_0$  was also measured with a VSM for all samples. These measurements are given in table 2. Errors of 22% and 26% resulted in the two trials.

### 3. Conclusions and Final Comments

The high drive field slew rates at which the loop operates have certain undesirable side effects. M-H traces exhibit distortion, which grows with slew rate. The apparent stripe-in field, coercive field and to a lesser extent, stripe collapse field are strongly influenced by slew rate. For sample 5804 the coercive field has been observed to vary from 3 to 40 Oe. The stripe in field varies from 10 to 100 Oe.

Delays in domain nucleation on the order of a few milliseconds and vibration of the drive field coils are believed to be the sources of this distortion. Slight movement of the sample and compensation coils (which are mounted on the drive field coils) result in an additional errant, coherent signal due to compensation bridge imbalance.

At a drive field frequency of 196.3 Hz,  $\chi_0$  quickly reaches a limiting value with decreasing slew rate for all samples tested. However,  $H_{sc}$  was still changing (although approaching the VSM value) as the drive field amplitude became too small to saturate the sample. Decreasing the drive field frequency by an order of magnitude would be a desirable modification of this device and allow measurement of  $H_{sc}$ .



TABLE 2

Comparison of VSM and M-H Looper Measurements for  $\chi_0$ 

Sample	Thickness $\mu\text{m}$	$\chi_0$	$\chi_0$
		VSM	Looper
5804	8.3	.113	$\equiv$ .113
5696	5.6	.0708	.0891
5692	5.19	.112	.137

In the device's present form noise considerations prohibit the use of samples with thickness less than about 5  $\mu\text{m}$ . Although successful loops from 2  $\mu\text{m}$  thick wafers have been recorded, the extremely noisy environment at WPAFB does not allow consistent performance. More careful shielding techniques, more sophisticated electronics and additional stiffening of the drive coil structure can overcome this limitation. Improvement in error figures should also be a result.

The information gained in this research was presented at the 24th Annual Conference on Magnetisms and Magnetic Materials at Cleveland, 14-18 November 1978 and published as "Two devices for non-optical characterization of full wafer magnetic bubble films" J. Appl. Physics 50 2182 (1979). The second device reviewed briefly in this paper is the microwave cavity technique for measuring bubble collapse and bubble stripe out fields. Details of the systems are discussed in the previous report #AFAL-TR-78-67.

## B. Spinwave Excitations in Domain Walls

During the past year, the theory explaining the absorption of microwave energy by unsaturated magnetic bubble materials was further developed. The work reported here is an extension of a paper presented<sup>(6)</sup> and of the previous year's annual report<sup>(7)</sup>. The propagation of spinwaves through a domain wall has previously been extensively considered<sup>(8-10)</sup>. In this analysis a single isolated 180° Bloch wall is considered in an infinite, lossless medium, with no external fields. The energy density consists of a bulk term, limited to the uniaxial anisotropy, given by

$$E^b = -K_u \sin^2\theta \cos^2\phi. \quad (7)$$

The demagnetization energy is ignored initially. The spherical coordinate system used is such that the  $r$  direction lies parallel to the equilibrium magnetization as shown in Figure 8.

For this system, the equation of motion for the magnetization, neglecting loss terms, can be written as

$$\frac{1}{\gamma} \frac{d\vec{M}}{dt} = \vec{\tau}^b + \frac{2A}{M_0^2} \vec{M} \times \nabla^2 \vec{M} \quad (8)$$

where the first term on the right hand side is the torque acting on the magnetization due to causes other than exchange. In general this may include such terms as the applied magnetic field, the crystalline stress and growth induced anisotropy, and magnetostatic effects. The second term is due to the exchange interaction between spins. The bulk torque term can be written as

$$\vec{\tau}^b = - \frac{\vec{M}}{M_0} \times \nabla E^b, \quad (9)$$

Here  $E^b$  is the bulk energy density excluding exchange effects.

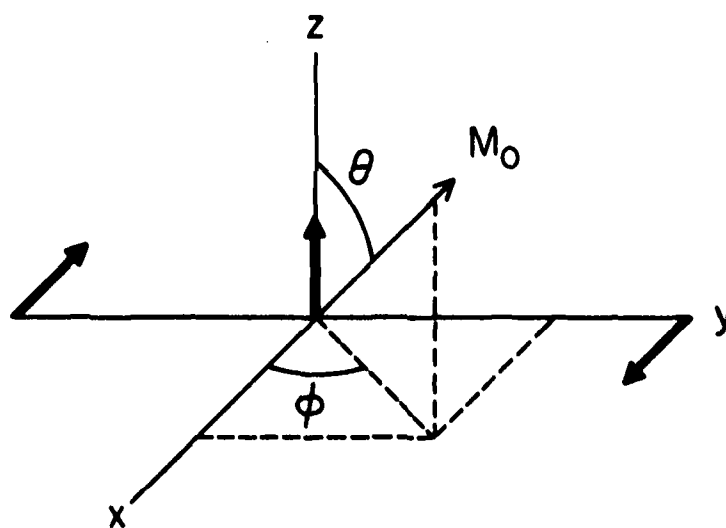


Fig. 8 Coordinate system used in the derivation of equation of motion. The domain wall is in the XZ plane. X is the film normal.

In the position dependant coordinate system used here the total magnetization is written as

$$M(y,t) = M_0 \hat{r}(y) + m_\theta(y,t) \hat{\theta}(y) + m_\phi(y,t) \hat{\phi}(y) \quad (10)$$

It is assumed that  $m_\theta \ll M_0$  and  $m_\phi \ll M_0$ . In this approximation

$$(M_0^2 - m_\theta^2 - m_\phi^2)^{1/2} \approx M_0. \quad (11)$$

For the coordinate system in Figure 8, a Bloch wall has  $\phi = \phi = 0$ . Then to first order in  $m_\theta$  and  $m_\phi$ ,

$$\begin{aligned} \vec{M} \times \nabla^2 \vec{M} = & (M_0 M_\phi \theta'^2) \hat{r} - [M_0 m_\theta (\theta')^2 + M_0 m_\phi''] \hat{\theta} + [-M_0 m_\theta (\theta')^2 + \\ & M_0^2 \theta'' + M_0^2 m_\phi' + M_0 m_\theta (\theta')^2] \hat{\phi}, \end{aligned} \quad (12)$$

where the primes represent differentiation with respect to  $y$ .

The equilibrium configuration is easily obtained by taking Eqn. 12 to the zeroth order in  $m_\theta$  and  $m_\phi$  and equating the right hand side of Eqn. 8 to zero<sup>(11)</sup>. The result is

$$\theta(\eta) = \text{gd}(\eta) = 2 \tan^{-1} (e^\eta) - \frac{\pi}{2}, \quad (13)$$

where  $\eta$  is the reduced variable  $\left(\frac{K_U}{A}\right)^{1/2} y$  and  $\text{gd}(\eta)$  is the Gudermanian function of  $\eta$ .  $\theta(\eta)$  is shown in Figure 9. The following identities between  $\theta$  and  $\eta$  also exist,

$$\cos \theta = \text{sech } \eta \quad \text{or} \quad \sin \theta = \tanh \eta. \quad (14)$$

Considering small deviations of the magnetization about the equilibrium position given by Eq. 13, the equations of motion for  $m_\theta$  and  $m_\phi$  can be derived<sup>(12)</sup>.

$$\begin{aligned} \frac{1}{\gamma} \frac{\partial m_\theta}{\partial t} = & E_\phi^b \csc \theta + \frac{1}{M_0} [m_\phi (E_\theta^b \cot \theta + E_\phi^b \csc^2 \theta) + \\ & m_\theta (E_\phi^b \csc \theta \cot \theta)] - \frac{2A}{M_0} [(\theta')^2 m_\phi + m_\phi^{11}] \end{aligned} \quad (15a)$$

$$\theta(\eta) = \text{gd}(\eta) = 2 \tan^{-1}(\bullet \eta) - \pi/2$$

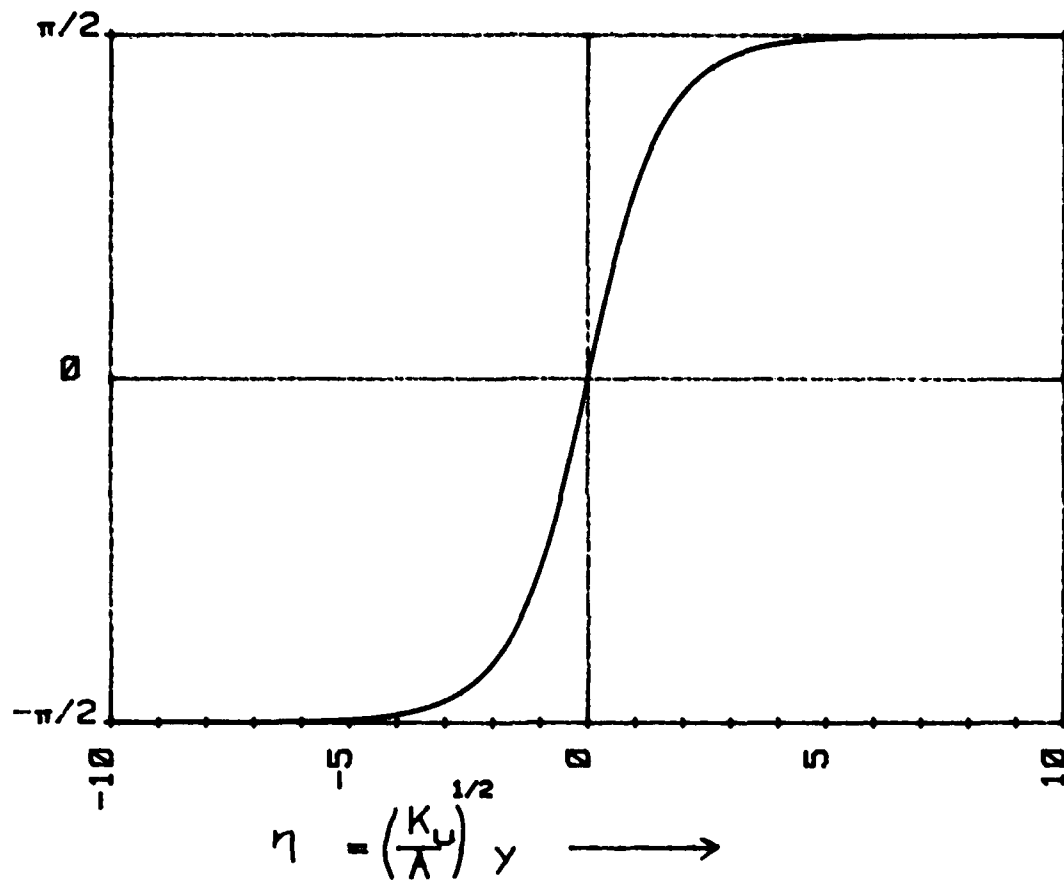


Fig. 9  $\theta$  as a function of the reduced variable  $\eta$ .

and

$$\frac{1}{\gamma} \frac{\partial m_\phi}{\partial t} = \frac{1}{M_0} [-m_\theta E_{\theta\theta}^b + m_\phi (E_\phi^b \cot\theta \csc\theta - E_{\theta\phi}^b \csc\theta)] + \frac{2A}{M_0} \theta$$

For the energy density in Eq. 7, the derivative terms are

$$\begin{aligned} E_\theta^b &= 2K_u \sin\theta \cos\theta, \\ E_\phi^b &= 0 \\ E_{\phi\phi}^b &= 0 \\ E_{\theta\theta}^b &= -2K_u \cos 2\theta \\ E_{\phi\phi}^b &= 2K_u \sin^2\theta \end{aligned} \quad (16)$$

Substituting these into Eq. 15 and using Eq. 14, the equations of motion reduce to

$$\frac{1}{\gamma} \frac{\partial m_\theta}{\partial t} = \frac{2K_u}{M_0} [(1 - 2\operatorname{sech}^2\eta)m_\phi - \ddot{m}_\phi],$$

and

$$\frac{1}{\gamma} \frac{\partial m_\phi}{\partial t} = \frac{-2K_u}{M_0} [(1 - 2\operatorname{sech}^2\eta)m_\theta - \ddot{m}_\theta],$$

where  $\ddot{m}_\theta$  represents the double derivative with respect to  $\eta$ ,

$$\ddot{m}_\theta = \frac{\partial^2(m_\theta)}{\partial \eta^2}$$

These two equations can be decoupled by defining new variables

$$m_\pm = m_\theta \pm im_\phi \quad (19)$$

The decoupled equations are

$$\frac{1}{\gamma} \frac{\partial m_+}{\partial t} = \frac{2K_u}{M_0} [(1 - 2\operatorname{sech}^2\eta)m_+ - \ddot{m}_+] \quad (20a)$$

and

$$\frac{1}{\gamma} \frac{\partial m_-}{\partial t} = \frac{-2K_u}{M_0} [(1 - 2\operatorname{sech}^2\eta)m_- - \ddot{m}_-] \quad (20b)$$

Since both  $m_\theta$  and  $m_\phi$  are real,  $m_+^* = m_-$  and Eqs. 20 are complex conjugates of each other. Assuming a time dependence of the form

$$m_\pm(t) = m_\pm e^{\pm i\omega t}, \quad (21)$$

the  $m_+$  equation can be written as

$$\frac{\partial^2 m_+}{\partial \eta^2} + [\Omega - 1 + 2\text{sech}^2 \eta] m_+ = 0 \quad (22)$$

where  $\Omega = \frac{\omega M_0}{2\gamma K_u}$ . Eqn. 22 is a Schrödinger like equation with a "potential"  $-2\text{sech}^2 \eta$ , which has a minimum at  $\eta = 0$  and goes to zero asymptotically as  $\eta \rightarrow \pm\infty$ . This is shown as a function of  $\eta$  in Figure 10.

Eqn. 22 can be solved exactly (10,13) with the solutions divided into two parts:

1) The Bound States: The bound state occurs at  $\Omega = 0$  with the eigenfunction  $m_\theta = \text{sech} \eta$ . Since  $m_\theta$  is equivalent to a change in  $\theta$ , one can write

$$m_\theta \propto \delta\theta = \delta \text{sech} \eta$$

where  $\delta$  is a proportionality constant. Then

$$\tanh \eta = \sin(\theta + \delta\theta) = \sin\theta + \delta\theta\cos\theta$$

or

$$\begin{aligned} \sin\theta &= \tanh \eta - \delta\theta\cos\theta \\ &= \tanh \eta - \delta \text{sech}^2 \eta \\ &= \tanh(\eta - \delta) \end{aligned}$$

which is a domain wall centered at  $\eta = \delta$ . Thus the bound state corresponds to a translation of the wall. For the general potential,  $-Q \text{sech}^2 \eta$ , there is only the one bound state at  $\Omega = 0$  for  $Q = 2$ . If  $Q$  were to be increased by a perturbation, another bound state would appear for  $\Omega$  slightly less than 1, this being very close to the continuum states.



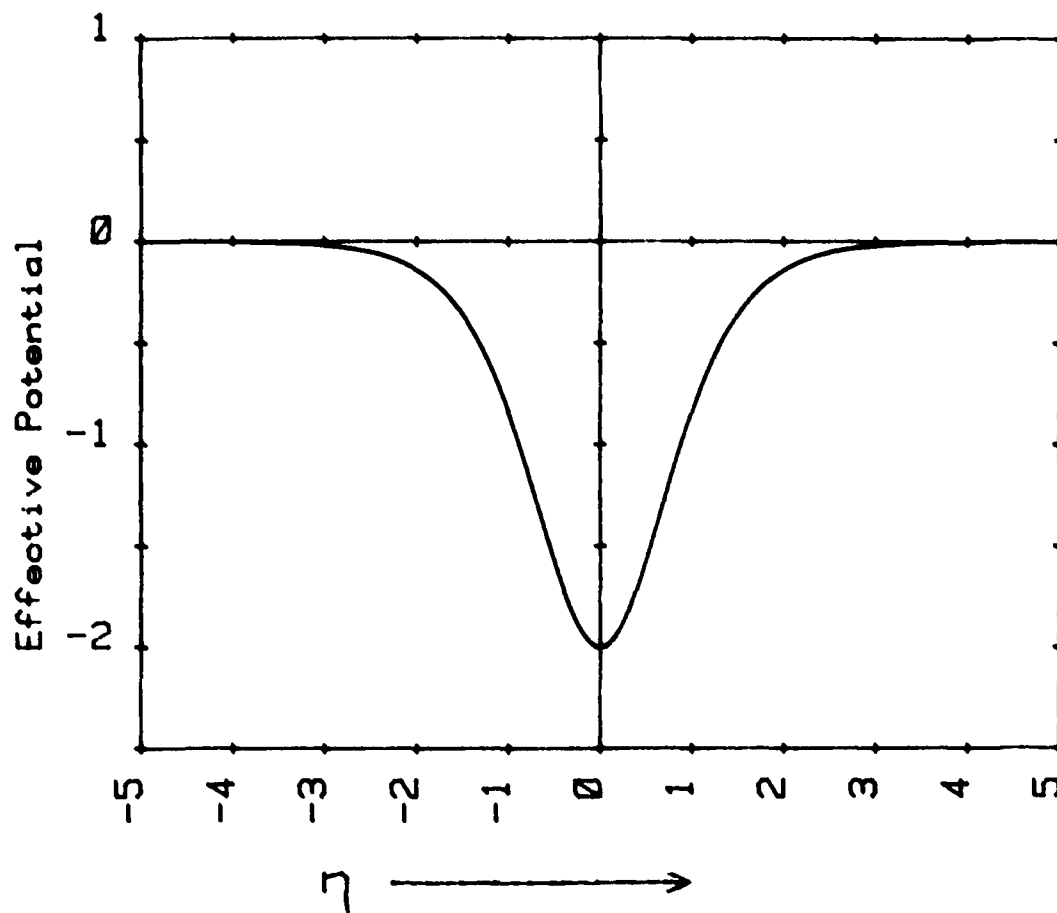


Fig. 10 The effective potential  $-2\text{sech} \cdot \eta$  as a function of  $\eta$  the dimensionless length variable.

2) The Continuum States: These appear for  $\omega > 1$  and the eigenfunction can be written as

$$m_0 = \frac{k + i \tanh \eta}{(1 + k^2)^{1/2}} \quad (23)$$

where  $k = \sqrt{\omega^2 - 1}$  and the real and imaginary parts of Eqn. 23 are two linearly independent solutions of Eqn. 22. The factor of  $(1 + k^2)^{-1/2}$  normalizes the solution so that far away from the wall solution takes the form

$$m = \cos(k\eta + \alpha)$$

where  $\alpha$  is a phase. This is a propagating spin wave valid for both  $m_0$  and  $m_\phi$ . The potential is completely transparent<sup>(9,10)</sup>. However, the domain wall distorts the propagating spin wave as shown in Figure 11 and develops a net r.f. magnetic moment. This r.f. moment couples with the microwave magnetic field, leading to absorption of energy. To calculate this coupling strength, it is necessary to normalize the solutions to obtain the amplitude of the propagating spin wave. Before normalizing, the inferences of the demagnetization energy will be considered.

The demagnetization energy is calculated in the Winter<sup>(8)</sup> approximation. The demagnetizing field is defined by the following equations

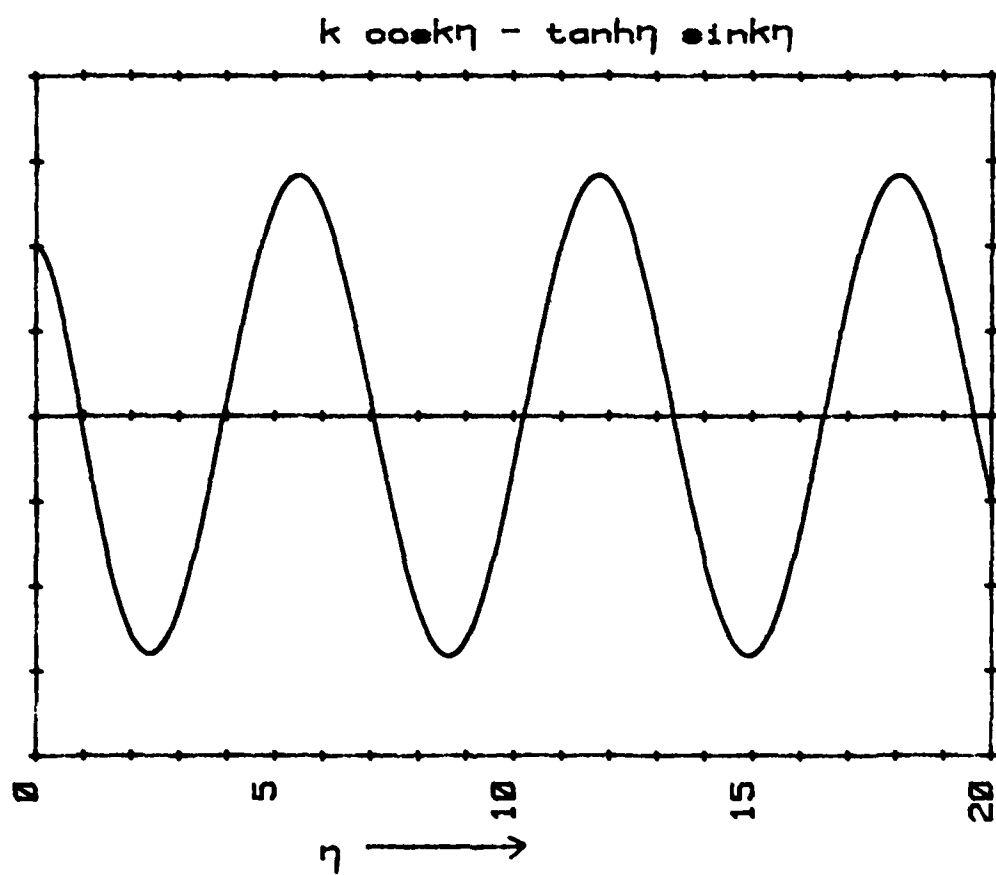
$$\nabla \cdot \vec{H}_d = -4\pi \nabla \cdot \vec{M}, \quad \nabla \times \vec{H}_d = 0 \quad (24)$$

Assuming slow spatial variation in the x and z directions, Eqn. 24 is approximately satisfied by

$$\vec{H}_d = -4\pi \vec{M}_y \hat{y} \quad (25)$$

The demagnetization energy then has the form

$$E_d^b = 2\pi \vec{M}_y^2 = 2\pi M_0^2 \sin^2 \theta \sin^2 \phi \quad (26)$$



$$m'_0 = 0$$

$$k \sin ka + \cos ka = 0$$

Fig. 11 Symmetric part of the spin-wave solution to Eq. (16).

Adding this to Eqn. 7 leaves all energy derivatives in Eqn. 16 unchanged except for  $E_{\phi\phi}^b$  which becomes

$$E_{\phi\phi}^b = 2K_u \sin^2 \theta + 4\pi M^2 \sin^2 \theta \quad (27)$$

The equations of motion now have the form

$$\frac{1}{\gamma} \frac{\partial m_\theta}{\partial t} = \frac{2K_u}{M_o} [(1 - 2\text{sech}^2 \eta) m_\phi - \ddot{m}_\phi] - 4\pi M_o m_\phi \quad (28)$$

and

$$\frac{1}{\gamma} \frac{\partial m_\phi}{\partial t} = \frac{-2K_u}{M_o} [(1 - 2\text{sech}^2 \eta) m_\theta - \ddot{m}_\theta] \quad (29)$$

These two equations do not readily decouple. Assuming a time dependence  $e^{i\omega t}$  and drawing on the experience with Eqn. 22, the following solutions are substituted into Eqns. 28 and 29.

$$m_\theta = B(k + i \tanh \eta) e^{ik\eta} \quad (30a)$$

and

$$m_\phi = C(k + i \tanh \eta) e^{ik\eta} \quad (30b)$$

$m_\theta$  and  $m_\phi$  are the real parts of Eq. 30. This leads to

$$\frac{i\omega}{\gamma} B = \frac{2K_u}{M_o} [1 + k^2 + \frac{2\pi M_o^2}{K_u}] C \quad (31a)$$

and

$$\frac{i\omega}{\gamma} C = \frac{-2K_u}{M_o} [1 + k^2] B \quad (31b)$$

To have non-trivial values of B and C

$$\Omega^2 = (1 + k^2 - \alpha)(1 + k^2), \quad (32)$$

where

$$\Omega = \frac{\omega M_o}{2\gamma K_u} \quad \text{and} \quad \alpha \equiv \frac{1}{Q} = \frac{2\pi M_o^2}{K_u}$$

Eqn. 32 can be solved for  $k^2$  giving

$$k^2 = \frac{1}{2} [-2 - \alpha \pm (\alpha^2 + 4\Omega^2)^{1/2}] \quad (33)$$

Only the upper sign is retained since when  $\alpha = 0$  (i.e. when demagnetization is ignored)  $k^2 = \Omega - 1$ . Thus the effect of the demagnetization energy is to change the value of  $k$  for a given frequency. For typical bubble films,  $\alpha \sim 0.1$ <sup>(15)</sup>. Thus for  $\Omega > 1$  the change is quite small. To calculate the coupling of these spin waves to an r.f. field applied in the xy plane (the plane of the film), and normal to the domain wall ( $h_{r.f.}/y$ ), the effect of the r.f. field is added to Eqns. 28 and 29. To first order in  $m_\phi$  and  $h_y$  (assuming  $h_y \ll \frac{2K_u}{M_0}$ ), Eqn. 29 is unchanged and Eqn. 28 has the following inhomogeneous form.

$$\frac{i\omega}{\gamma} m_\theta = \frac{2K_u}{M_0} [(1 - 2\text{sech}^2\eta)m_\phi - \ddot{m}_\phi] - 4\pi M_0 m_\phi + M_0 h_y \quad (34)$$

A solution of the form

$$m_\theta = \sum_k B_k (k \cos k\eta - \tanh \eta \sin k\eta) = \sum_k B_k \psi(k, \eta) \quad (35)$$

is assumed. The allowed values of  $k$  are discussed below. This solution is symmetric about the origin. The other form of the solution ( $k \sin k\eta + \tanh \eta \cos k\eta$ ) is antisymmetric and will not give rise to a net moment since the inhomogeneous term in Eqn. 34 is symmetric.  $m_\phi$  would be given as a sum in terms of  $C_k$ , related to  $B_k$  by Eqn. 31.

In order to evaluate  $B_k$ , certain boundary conditions are required to make solutions belonging to different  $k$  values orthogonal. The condition  $m'_\theta = 0$  at  $\eta = \pm a$ , where  $a \gg \delta$ , the wall thickness, is used. Since the spin waves are essentially "free" far away from the wall, the boundary conditions are only a mathematical convenience facilitating the calculation of the  $k$  dependence of the r.f. moment.

The present choice insures that  $\int_{-a}^a m_y d\eta$  equals the total moment generated at the wall. The actual value of  $a$  is not predicted in this model and was used as a fitting parameter. Due to the presence of damping in the sample the spin waves excited at one domain wall decay before reaching the next wall (except for small  $k$ ). Thus the domain walls are essentially isolated. This is achieved, in this model, by the boundary conditions and the value of  $a$  giving the best fit reflects the amount of damping present. This boundary condition puts restriction on the allowed value of  $k$ :

$$k \sin ka + \cos ka = 0. \quad (36)$$

With these boundary conditions, the solutions of Eqn. 34 belonging to various values of  $k$  are orthogonal (self adjoint differential equation with Neuman boundary conditions). Eqn. 35 and a similar relation for  $m_\phi$ , together with Eqns. 34 and 31 lead to

$$\sum_k B_k [(1 + k^2 + \alpha)(1 + k'^2) - \Omega_0^2] \psi(k, \eta) = \frac{M_0^2 h y}{2K_u}, \quad (37)$$

where  $\Omega_0$  corresponds to the applied field frequency. Setting  $(1 + k^2 + \alpha)(1 + k'^2) = \Omega^2$ , and using the orthogonality of the  $\psi$ 's, namely

$$\int_{-a}^a \psi(k, \eta) \psi'(k', \eta) d\eta = \delta_{kk'} \int_{-a}^a \psi^2(k, \eta) d\eta, \quad (38)$$

where both  $k$  and  $k'$  satisfy Eqn. 36, the following relation for  $B_k$  is obtained.

$$B_k = \frac{iM_0^2 h y \left[ \int_{-a}^a \psi(k, \eta) d\eta \right]^2}{(\Omega^2 - \Omega_0^2) \left[ \int_{-a}^a \psi^2(k, \eta) d\eta \right]} \cdot \frac{\Omega_0}{2K_u} \quad (39)$$

A similar relation can be written for  $C_k$ , using Eqn. 31.

The component of the moment in the r.f. field direction associated with a sample of thickness  $\tau$  and area  $A_s$  is

$$M_{d \cdot w} = \vec{m} \cdot \vec{h}_{rf} dv = \int_{-a}^a C_k \psi(k, \eta) d\eta \cdot \frac{2A_s \tau}{P_0} =$$

$$\frac{2A_s \tau M_0^2 h y}{P_0 (\Omega^2 - \omega_0^2)} \cdot \frac{\left[ \int_{-a}^a \psi(k, \eta) d\eta \right]^2}{\left[ \int_{-a}^a \psi^2(k, \eta) d\eta \right]} \cdot \frac{(1+k^2)}{\Omega} \quad (40)$$

where  $P_0$  is the stripe period at zero bias field. This factor is necessary due to the periodicity of the domain walls present. In the experiment this moment is compared with the r.f. moment of the uniform mode for which<sup>(14)</sup>

$$M_u = \frac{2a \gamma M_0^2 h y}{\omega^2 - \omega_0^2} \quad (41)$$

The power absorbed by the sample in each mode is proportional to the corresponding moment. Hence the ratio of the power absorptions is given by

$$R = \frac{M_{dw}}{M_u} = \frac{2 \left[ \int_{-a}^a \psi(k, \eta) d\eta \right]^2}{P_0 \left[ \int_{-a}^a \psi^2(k, \eta) d\eta \right]} \cdot \frac{1+k^2}{\Omega} \quad (42)$$

Here  $\Omega$  has been set equal to  $\omega_0$ . This does not indicate a resonance. In the experiment it is assumed that only the modes with the same frequency as that of the driving r.f. field are excited, leading to power absorption at that frequency; thus justifying  $\Omega = \omega_0$  and  $k = k_0$ .

The integrations in Eq. 42 were performed numerically. Similar calculations for  $\vec{h}_{rf}$  parallel to the Z axis give a ratio two orders

of magnitude smaller. Eq. 42 predicts only the  $k$  dependence of the intensity ratio. The actual magnitude of the ratio depends on the choice of  $a$ , which is not determined in this theory. Hence  $a$  is used as a fitting parameter.

According to Eq. 40, the domain wall moment changes as the inverse of the stripe period. As the bias field is increased, the stripe pattern changes and the stripe period,  $P$ , increases. The change in the demagnetization field can be assumed to cancel the change in the bias field. Thus to the first order, it can be assumed that the domain wall structure remains unchanged and the only effect of the bias field is to change  $P$ .

According to this picture, the domain wall signal should change as  $1/p$  as a function of the bias field. Starting with Eqns. 2 and 3 of Kooy and Enz.(16) the following relations are obtained.

$$\frac{1}{h} = -\frac{2M}{\pi^3\beta} \sum_{n=1}^{\infty} \frac{1}{n^3} \sin^2 \left[ \frac{n\pi}{2} \left( 1 + \frac{M}{M_S} \right) \right] \left[ \frac{n\pi\mu}{F^2} - \frac{\sinh n\pi\beta}{\beta F} \right] \quad (43)$$

and

$$\frac{H}{4\pi M_S} = \frac{M}{M_S} + \frac{2\sqrt{\mu}}{\pi^2\beta} \sum_{n=1}^{\infty} \frac{1}{n^2} \sin \left[ n\pi \left( 1 + \frac{M}{M_S} \right) \right] \left[ \frac{\sinh n\pi\alpha}{F} \right] \quad (44)$$

where

$$\mu = 1 + \frac{4\pi M_S}{H_u}$$

$$H_u = \frac{2Ku}{M_S}$$

$$F = \sinh(n\pi\beta) + \sqrt{\mu} \cosh(n\pi\beta)$$

$$\beta = \frac{\tau\sqrt{\mu}}{P}$$

$$P = d_1 + d_2$$



is the film thickness.  $d_1$  and  $d_2$  are the widths of the domains with the magnetization parallel and antiparallel to the bias field, respectively.

Eqns. 43 and 44 are solved numerically to give  $d_1 + d_2$  as a function of  $H$ . The program used on the HP 9825 is listed in Appendix C. Fig. 12 shows  $1/P$  as a function of  $H$ , along with the integral of the actual domain wall signal for the sample, Sperry 4/3/77-1. (Actual signal is derivative of the power absorption). The former was scaled to match the integrated signal at  $H=0$ . The agreement between theory and experiment is excellent. Indicating that a single domain wall model, such as the present one, is adequate to explain the shape of the observed low field signal.

#### EXPERIMENTAL

During the past year, spectrometers operating at c-band (6 GHz) and  $K_u$ -band (13.5 GHz) were constructed. Using these, data were taken on a number of samples. FMR data was taken at X-band as a function of the angle between  $H_{app}$  and the film normal. The data were fitted to the dispersion relation for a (111) oriented film:<sup>(17)</sup>

$$H_p \cos(\alpha - \alpha) = 2\pi M(\cos^2 \alpha + \cos 2\alpha) - \frac{1}{2} (g_1(\alpha) + g_2(\alpha)) + \frac{1}{2} \left\{ [4\pi M(\cos^2 \alpha - \cos 2\alpha) + g_2(\alpha) - g_1(\alpha)]^2 + 4\left(\frac{\omega}{\gamma}\right)^2 \right\}^{1/2} \quad (45)$$

$$\begin{aligned} g_1(\alpha) &= H_u \left[ \frac{1}{8} \sin^2 2\alpha - \frac{2}{3} \cos^4 \alpha - \frac{\sqrt{2}}{2} \sin 2\alpha \left( 1 + \frac{2}{3} \sin^2 \alpha \right) \right] \\ g_2(\alpha) &= H_u \left[ \frac{1}{12} \cos 2\alpha + \frac{7}{12} \cos 4\alpha + \frac{\sqrt{2}}{6} (\sin 2\alpha - 2 \sin 4\alpha) \right] \\ g_3(\alpha) &= H_u \left[ \frac{1}{24} \sin 2\alpha (1 + 7 \cos 2\alpha) - \frac{\sqrt{2}}{6} \sin^2 \alpha (1 + 2 \cos 2\alpha) \right] \end{aligned} \quad (46)$$

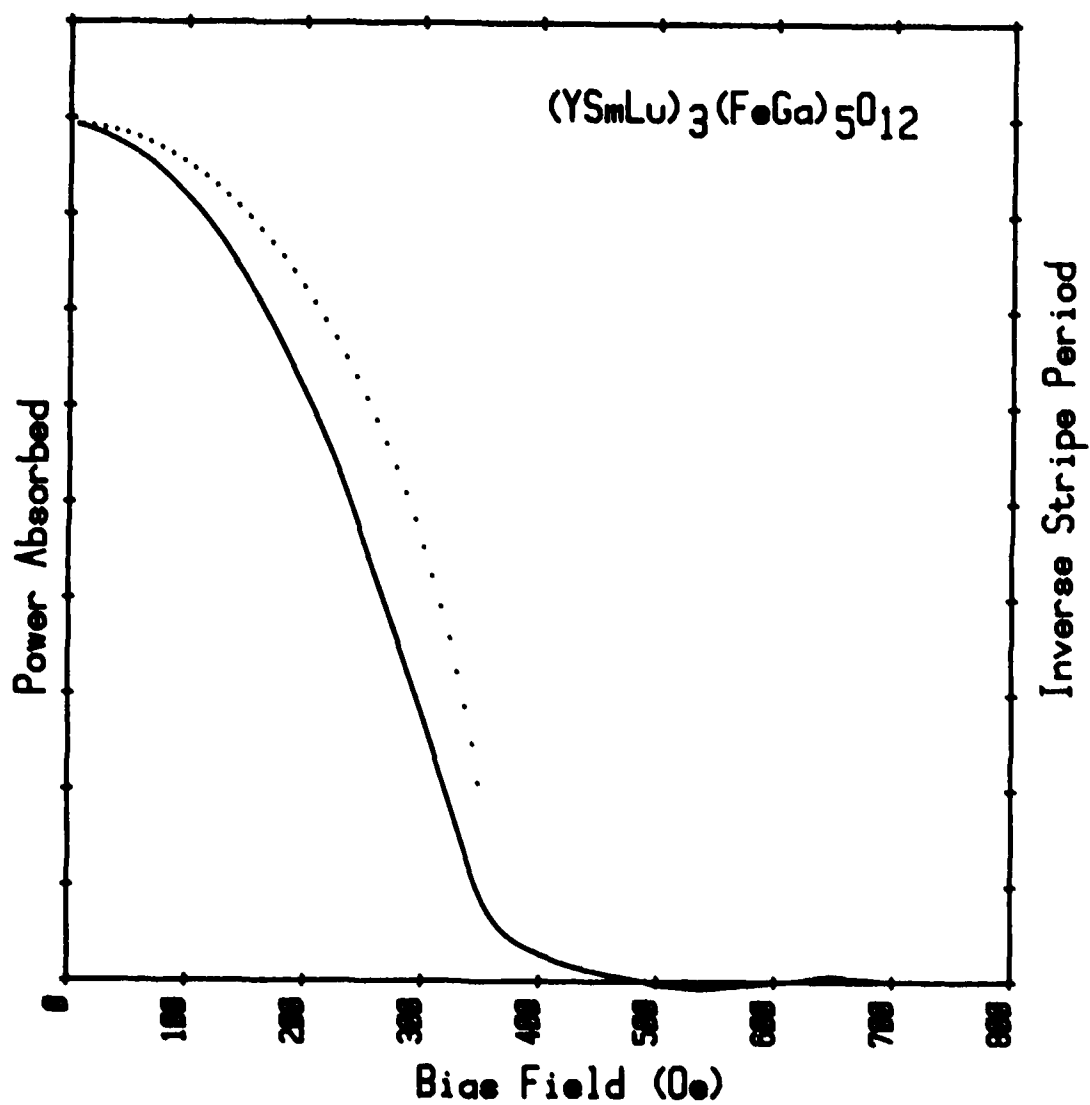


Fig. 12 solid line: Integral of the low field signal after subtracting the base line due to the uniform mode.

Dotted line: The inverse stripe period scaled to match the solid line at zero field.

$H_r$  is the field position of the uniform mode and  $\beta$  is the angle between  $H_{app}$  and the film normal. The sample is oriented so that  $H_{app}$  lies in the (110) Plane. The angle  $\alpha$ , between  $M$  and the film normal, is determined by the equation

$$H \sin(\beta - \alpha) + 2\pi M \sin 2\alpha + g_3(\alpha) = 0 \quad (47)$$

The data was fitted to this relation using a generalized least squares fitting routine<sup>(18)</sup> run on the 9825 computer. A listing of this program is included in Appendix D. This program gives the values of  $4\pi M - H_u$ ,  $\frac{\omega}{\gamma}$ , and  $H_k$ . The thickness used was that supplied with the sample.  $M$  was determined using the VSM and  $A$  was obtained through the characteristic length determined from a measurement of the stripe period<sup>(19)</sup>. Knowing the material parameters makes it possible to compare domain wall data with the theory.

Following the above procedure data were taken on a number of samples. One sample (3-18-16) was studied at C, X, and  $K_u$ -band to provide experimental data as a function of frequency. The results of these studies were reported at the AIP meeting in San Francisco in January 1978<sup>(20)</sup>.

To obtain more data on the frequency dependance implied by Eq. 42, the domain wall and uniform mode signals were studied in the temperature range 180K - 300K at X-band for the sample Sperry 4/3/77-1. As the temperature is lowered,  $H_u$  increases thus decreasing  $\omega$ . Thus experimental values for  $R$  could be obtained as a function of  $\omega$ , though the actual frequency remained constant. The temperature dependance of  $4\pi M$  was studied on the VSM and values of  $P_0$  in this temperature range were obtained by using a cold stage assembly on the Reichert microscope.  $P_0$  was found to be independent of temperature within the accuracy of the measurements.

In Fig. 13, the reduced ratio  $\frac{R\Omega'}{(1+k^2)}$  is plotted as a function of the wave vector  $k$ . In Eqn. 42 the right hand side is dependant on temperature due to the factor  $\frac{1+k^2}{\Omega}$  which by Eqn. 32 is  $\frac{1}{(1+k^2-\alpha)}$ , and  $\alpha$  changes with temperature. To correct this, the factor  $\frac{\Omega}{(1+k^2)}$  is included in the L, H, S and this reduced ratio is plotted. Also shown are the experimental points, indicating a very good agreement with the theory. These results were presented in the MMM Conference in Cleveland in November<sup>(6)</sup>. The parameters are listed in Table 3 & 4.

TABLE 3:  
MATERIAL PARAMETERS

Sample: Sperry 4/3/77-1  
Composition:  $(Y\text{SmLu})_3(\text{FeGa})_5\text{O}_{12}$   
h(thickness): 3.1  $\mu\text{m}$   
 $P_0$ (stripe period): 3.6  $\mu\text{m}$

TABLE 4

## EXPERIMENTAL RESULTS

T	$4\pi M(\text{Oe})$	$H_u(\text{Oe})$	$H_k(\text{Oe})$	$\omega/\gamma(\text{Oe})$	$\Omega$	$\lambda$	Expt. Ratio	Theory Ratio
299	556	1030	36	3214	3.12	1.36	$1.25 \times 10^{-3}$	$2.79 \times 10^{-4}$
290	568	1124	56	3203	2.85	1.27	$1.11 \times 10^{-3}$	$3.15 \times 10^{-4}$
275	617	1286	47	3187	2.48	1.12	$1.48 \times 10^{-3}$	$6.28 \times 10^{-4}$
265	655	1412	80	3163	2.24	1.01	$2.18 \times 10^{-3}$	$1.02 \times 10^{-3}$
255	677	1501	93	3150	2.10	0.94	$2.49 \times 10^{-3}$	$1.37 \times 10^{-3}$
245	701	1590	118	3130	1.97	0.87	$4.22 \times 10^{-3}$	$1.90 \times 10^{-3}$
235	738	1724	150	3109	1.80	0.78	$5.92 \times 10^{-3}$	$2.83 \times 10^{-3}$
225	772	1878	238	3064	1.63	0.66	$6.12 \times 10^{-3}$	$5.25 \times 10^{-3}$
215	792	2025	279	3028	1.50	0.56	$1.16 \times 10^{-2}$	$9.35 \times 10^{-3}$
205	807	2187	365	2966	1.36	0.43	$2.27 \times 10^{-2}$	$1.80 \times 10^{-2}$
195	829	2378	464	2916	1.23	0.25	$4.42 \times 10^{-2}$	$3.71 \times 10^{-2}$
185	854	2575	590	2822	1.10	0.23	$6.90 \times 10^{-2}$	$5.93 \times 10^{-2}$

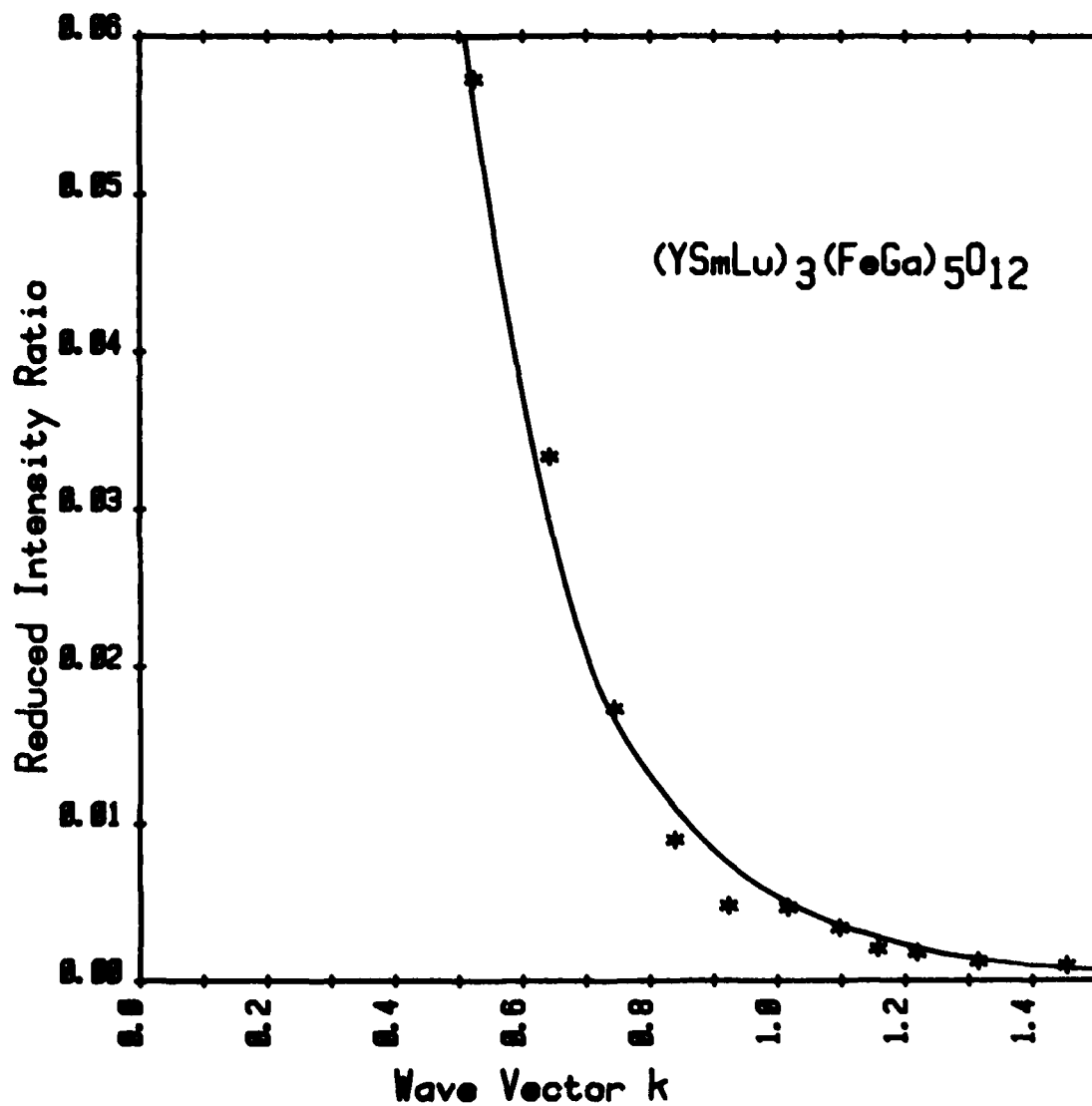


Fig. 13 The reduced intensity ratio  $R\omega/(1+k^2)$  as a function of the wave vector  $k$ . The solid line shows the theoretical calculations. The data points are shown by astericks. Data was taken at  $9.2 \text{ GHz}$ . Best fit was obtained for  $a=0.3 P_0$ .

### C. Radio Frequency Domain Wall Oscillations

During the first part of the past year, data was taken on a variety of samples at a variety of frequencies using the RF spectrometer described in the previous annual report<sup>(7)</sup>. Data obtained from 7 different samples at frequencies from 5 MHz to 100 MHz show a low field power absorption characteristic of the presence of domains. This broad band characteristic indicates that the effect being observed is not the bound spin wave state expected when this project was initiated. This conclusion is further supported by the failure of the calculations reported in another section B of this report to predict bound states in this frequency range ( $.0035 \leq \omega \leq .03$ ). Considerable effort has been expended in an attempt to understand the nature of the coupling of the in-plane RF magnetic field to the domains.

In addition to the above mentioned work, some studies of the operating characteristics of the spectrometer have been undertaken. Of particular interest were signal strength vs. input RF power and signal strength vs. bridge isolation. As shown in Figs. 14 & 15, the signal strength varies directly with RF power and seems to be independent of isolation. Experiments were also performed by operating the spectrometer as a direct absorption spectrometer, dispensing with the modulation field and lock-in amplifier. A typical spectrum taken in this mode is illustrated in Figure 16.

As data was taken on a number of samples, it became evident that it would be desirable to be able to measure the frequency dependence of the domain wall signals. This is not practical with the type of spectrometer initially used as its tuning is very narrow band (see Fig. 17). This narrow band characteristic is a direct result of using a resonant coil to couple the rf magnetic field into the sample, so the decision was made to modify the spectrometer to operate in a non-resonant manner

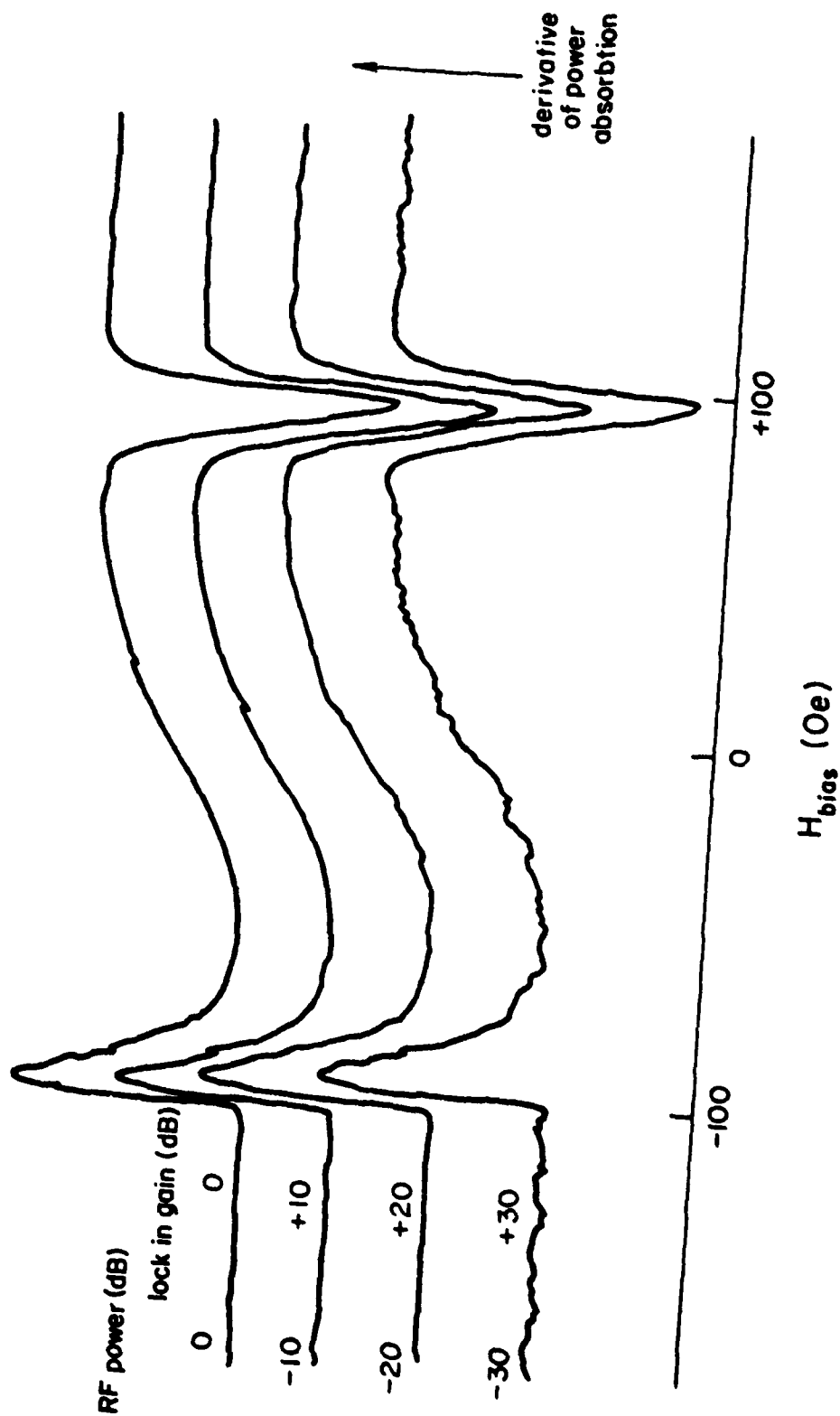


Fig. 14 Signal Strength and S/N as a function of RF power



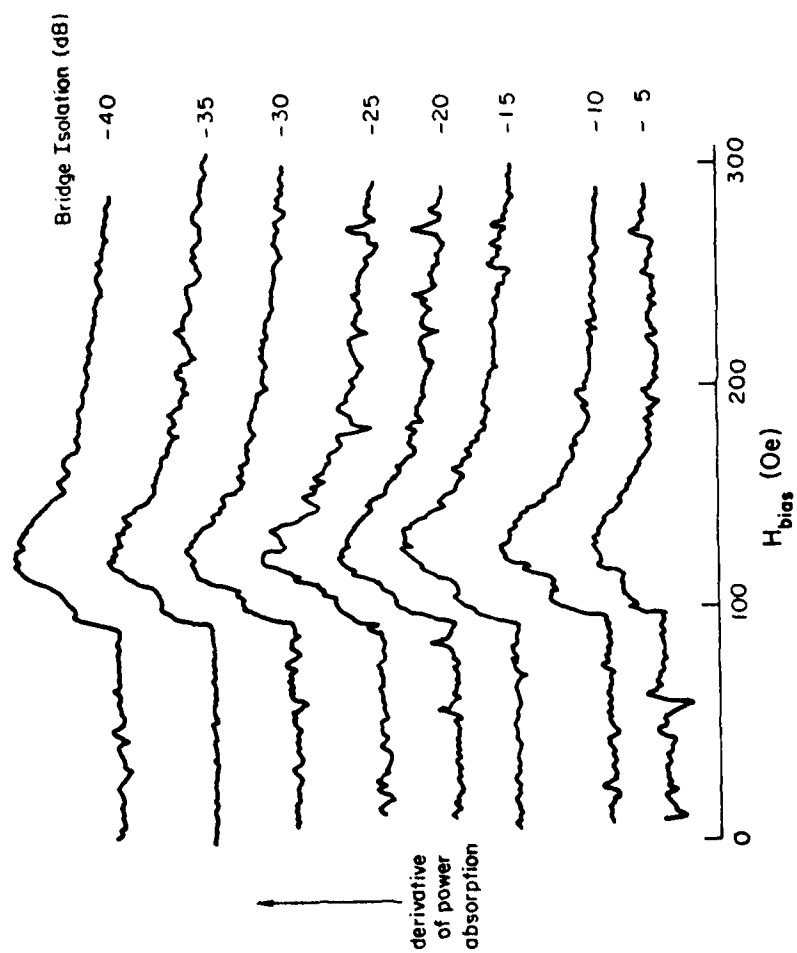


Fig. 15 Signal Strength and S/N as a function of Bridge isolation.

Direct Absorption Spectrum  
Sample TI330 98.61 MHz

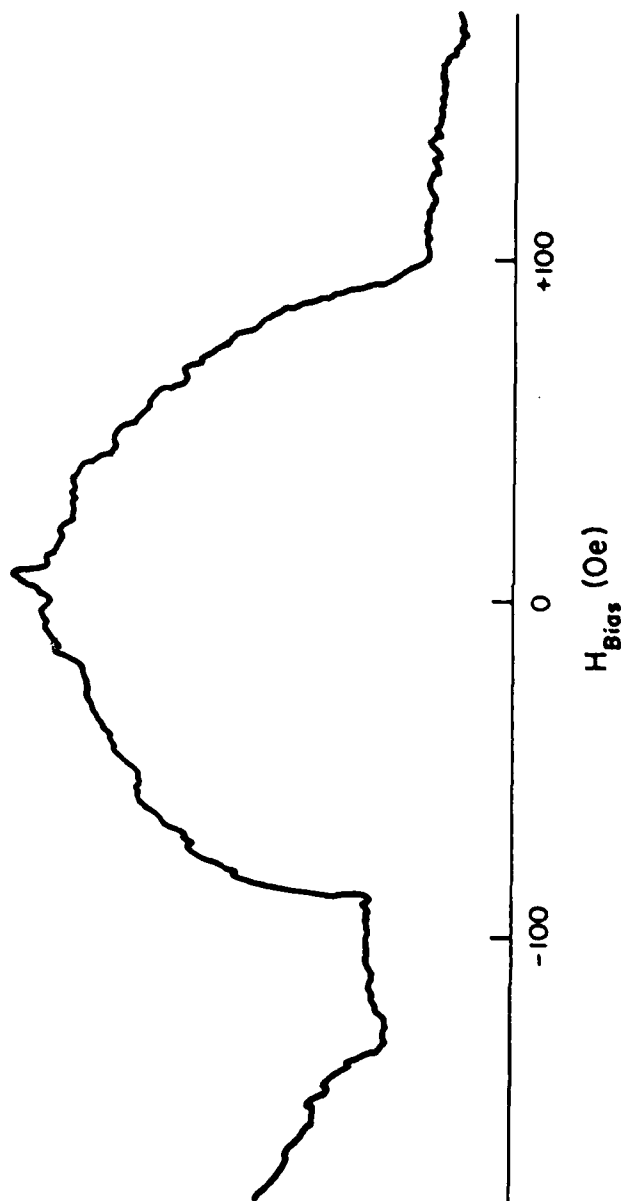


Fig. 16 Typical direct absorption spectrum

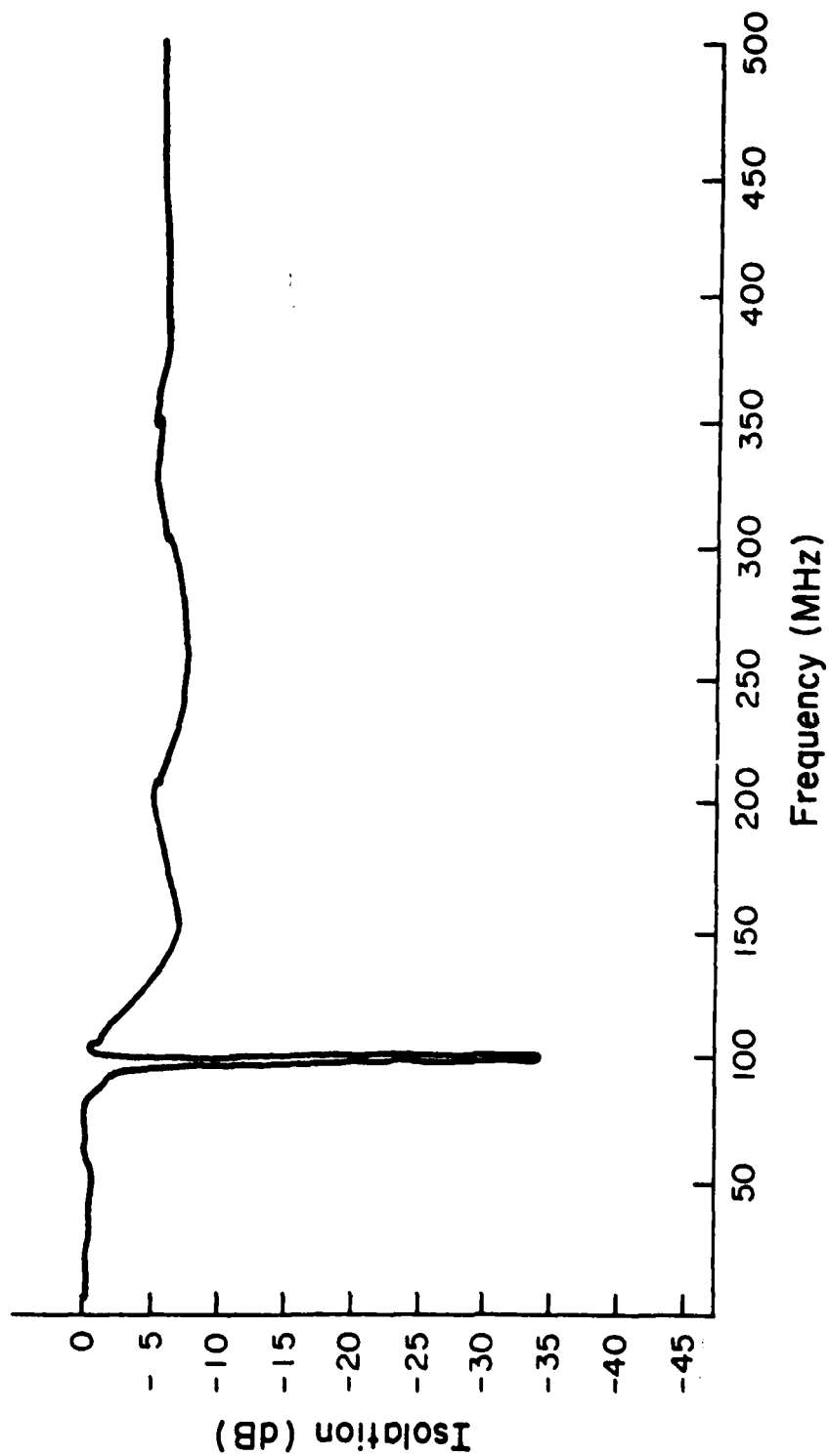


Fig. 17 Bridge isolation vs. frequency-resonator type spectrometer.  
Spectrometer will only operate when isolation is -5dB or greater.

thus enabling swept frequency measurements. The method adopted is to replace the tuned coil entirely with a transmission line having a helical center conductor and terminated in its characteristic impedance. This system operates in the spectrometer in exactly the same manner as the tuned coil, provided its characteristic impedance was equal to the impedance of the terminator on the opposite arm of the bridge. The advantage to this system is that it requires no modification to the rest of the spectrometer, except the addition of a swept signal generator as the rf source.

The design of the helical transmission line is shown in Fig. 18 and is based on the characteristic impedance of such a device, given by

$$Z_0 = \frac{.030n^2d^2(1-(\frac{d}{D})^2) \log \frac{D}{d}}{7.4 \epsilon_r} \quad (48)$$

where  $n$  is the pitch of the helix in turns/inch,  $d$  is the diameter of the helix in inches, and  $D$  is the diameter of the outer conductor in inches<sup>(2)</sup>. Constraints were placed on the design by machining limitations. The values of the parameters used were  $n = 20$  turns/in.,  $d = .704$  in., and  $D = .785$  in., giving a designed impedance of 50  $\Omega$ . Copper magnet wire (28 ga) was used to form the helix itself. Due to assembly difficulties,  $d$  was decreased during assembly to .684 in., changing the theoretical impedance to 60  $\Omega$ . After assembly, the frequency characteristics and impedance were measured. Using a pulse technique, the characteristic impedance of the helical line was found to be 200  $\Omega$ . A plot of its frequency response is indicated in Figure 19. Due to the serious mismatch between the helix and the rest of the system, a resistive impedance matching network was designed to match the helix to 50  $\Omega$ . This device works very well, and the response of the system with the helix on the bridge is shown in Figure 20.

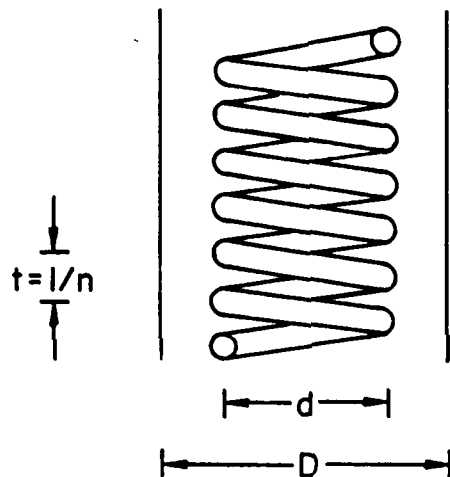


Fig. 18 Diagram of a short section of helical transmission line.

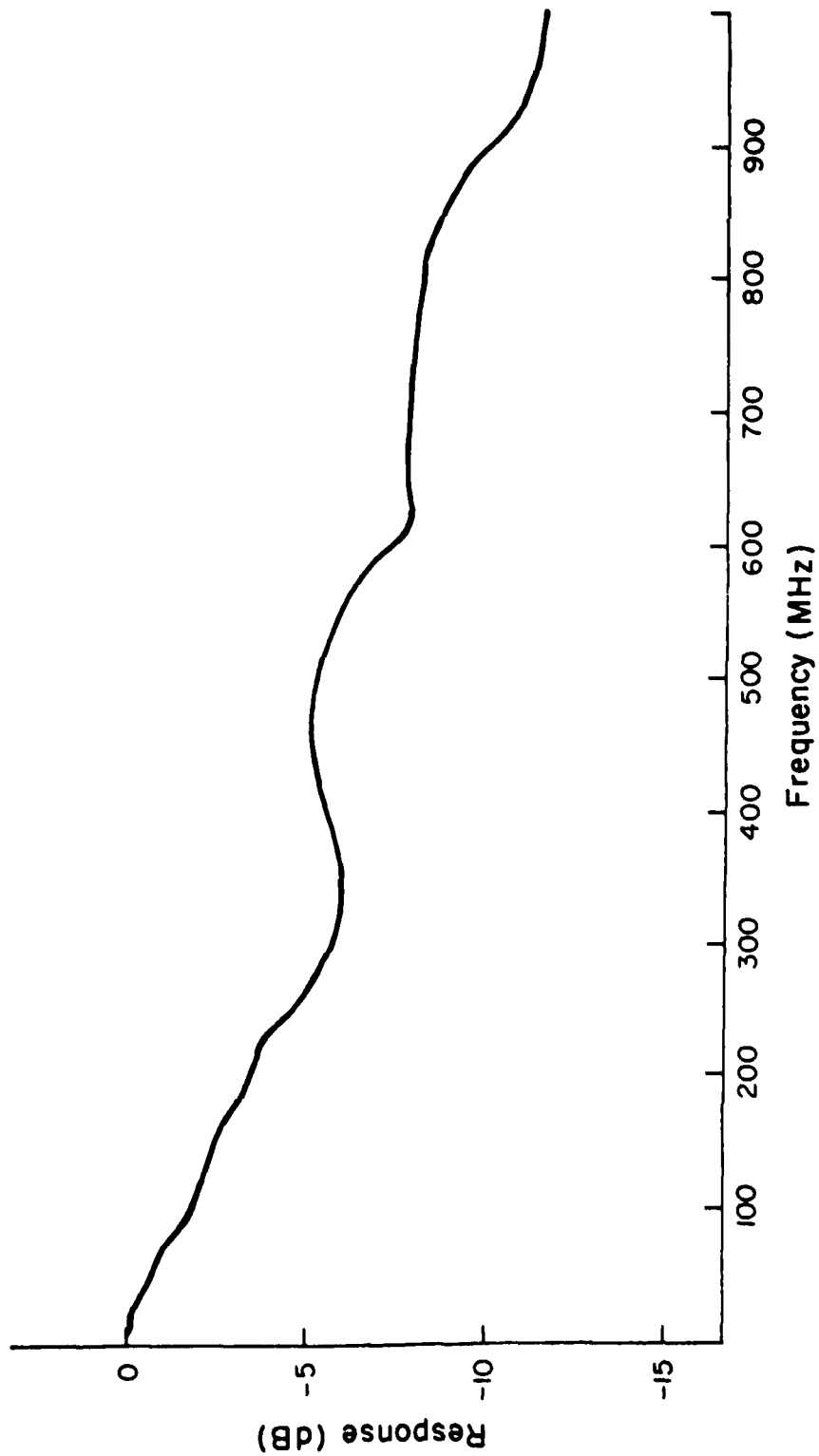


Fig. 19 Frequency response of helical transmission line

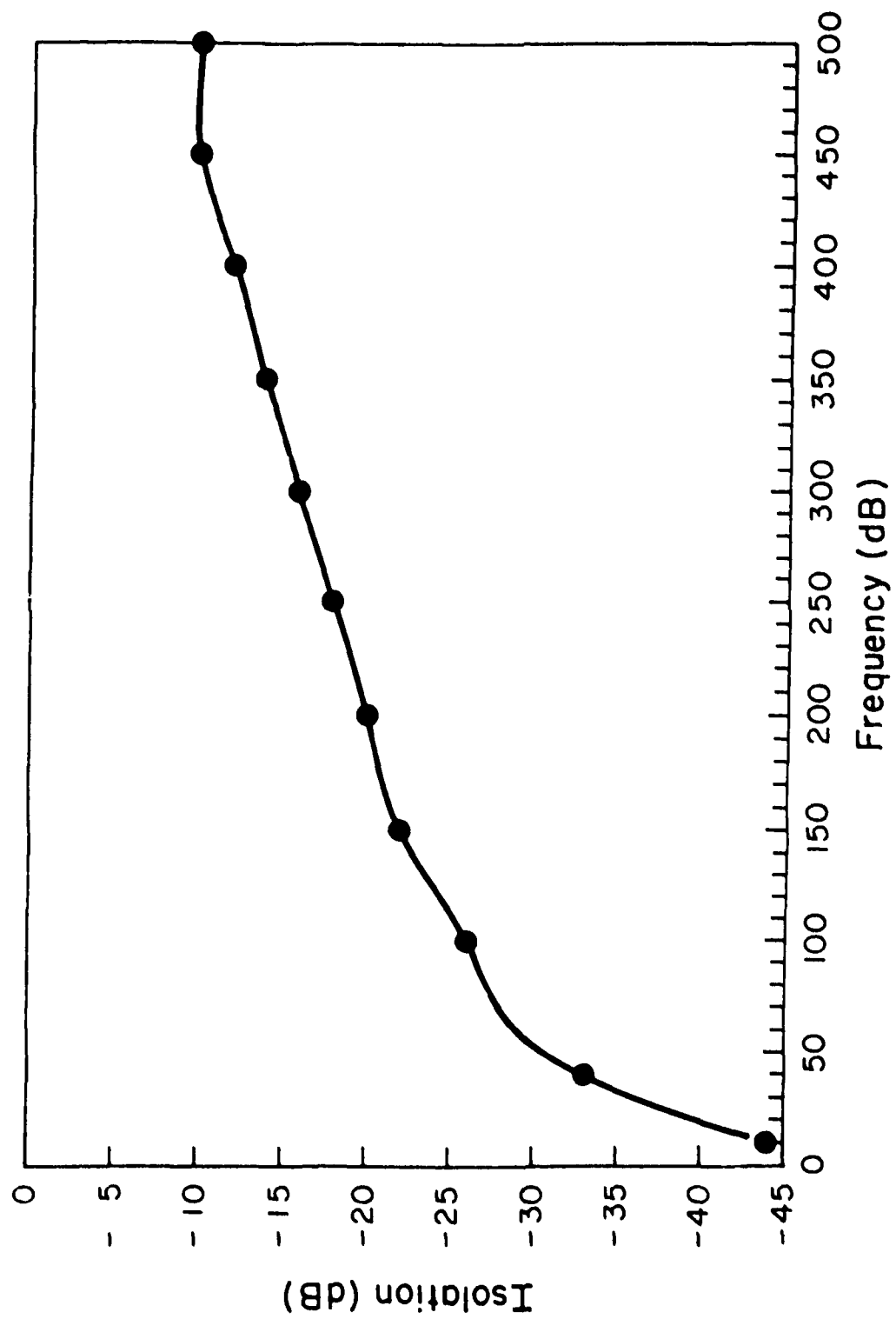


Fig. 20 Frequency Response-Spectrometer with helical transmission line and matching network.

To date, no data has been taken with this device and work is continuing toward assembly and use of a spectrometer using this device.

## 2: Theory

Drawing on work done by Slonczewski<sup>(22)</sup>, the generalized equations of motion for a domain wall are

$$\frac{\delta \mathcal{O}}{\delta \psi} = \frac{2M}{\gamma} (\dot{q} - \alpha \Lambda \dot{\psi}) \quad (49)$$

$$\frac{\delta \mathcal{O}}{\delta q} = -\frac{2M}{\gamma} (\dot{\psi} + \frac{\alpha}{\Lambda} \dot{q})$$

Here  $q$  is the wall position,  $\psi$  is the angle of the magnetization with respect to the  $x$  axis,  $\alpha$  is the Gilbert damping coefficient for the material,  $\Lambda$  is the wall width parameter ( $\Lambda = (\frac{A}{K_u})^{1/2}$ ), and  $\mathcal{O}$  is the energy density of the wall. The coordinate system used is shown in Fig. 21. The functional derivative  $\frac{\delta \mathcal{O}}{\delta q}$  is defined by

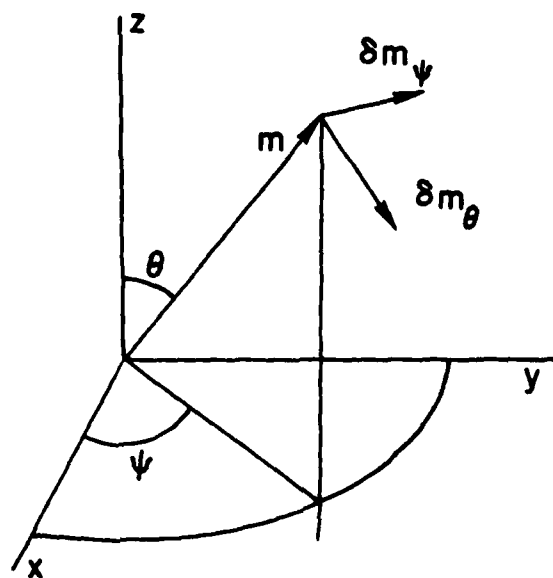
$$\frac{\delta \mathcal{O}}{\delta q} = \frac{\partial \mathcal{O}}{\partial q} - v \cdot \frac{\partial \mathcal{O}}{\partial \nabla q} \quad (50)$$

Including terms to account for exchange, uniaxial anisotropy, demagnetization and ground state energy, the variation of the energy density becomes

$$\begin{aligned} \delta \mathcal{O} = \delta \left\{ \frac{2A}{\Lambda} (vq)^2 + 2A\Lambda (v\psi)^2 + 4\pi M^2 \Lambda \sin^2(\psi - \frac{\partial q}{\partial x}) \right\} + \\ \pi M \Lambda (H_x \sin \psi - H_y \cos \psi) \delta \psi - 2MH_z \delta q \end{aligned} \quad (51)$$

where  $H_x$ ,  $H_y$ , and  $H_z$  are the cartesian components of the applied magnetic field and  $v = \hat{x} \frac{\partial}{\partial x} + \hat{z} \frac{\partial}{\partial z}$ .





Fixed coordinate system  $xyz$

Fig. 21 Fixed coordinate system  $xyz$

Performing the functional derivatives as indicated in Eqn. (49) and rearranging the resulting equations gives

$$\Delta^{-1} \dot{q} = 2\pi M \gamma \sin 2(\psi - \frac{\partial q}{\partial x}) + \frac{\pi \gamma}{2} (H_x \sin \psi - H_y \cos \psi) - \frac{2\gamma A}{M} \nabla \psi + \alpha \dot{\psi} \quad (52)$$

$$\dot{\psi} = \gamma H_z - 2\pi M \gamma \Delta \frac{\partial}{\partial x} (\sin 2(\psi - \frac{\partial q}{\partial x})) + \frac{2A\gamma}{M\Delta} \nabla^2 q - \frac{\alpha}{\Delta} \dot{q}$$

To a first approximation,  $\nabla q = \nabla \psi = 0$  at the center of a thin film. Also, if the x axis lies in the plane of the wall,  $\frac{\partial q}{\partial x} = 0$ . These two approximations simplify Eqn. (52) so that it becomes

$$\Delta^{-1} \dot{q} = 2\pi M \gamma \sin 2\psi + \frac{\pi \gamma}{2} (H_x \sin \psi - H_y \cos \psi) + \alpha \dot{\psi} \\ \dot{\psi} = \gamma H_z - \frac{\alpha}{\Delta} \dot{q} \quad (53)$$

If there is no bias field ( $H_z = 0$ ) and  $H_x = H_y = 0$  at  $t = 0$ , the initial conditions are  $q(0) = \psi(0) = 0$  and the equation for  $\psi$  can be solved as a function of  $q$

$$\psi(t) = -\frac{\alpha}{\Delta} q(t) \quad (54)$$

Thus, Eqn. (53) becomes a single, first order differential equation

$$\dot{q} = -[\frac{\Delta}{1+\alpha^2} 2\pi M \gamma \sin(\frac{2\alpha}{\Delta} q) + \frac{\pi \Delta \gamma H_{rf}}{2(1+\alpha^2)} \cos(\frac{\alpha}{\Delta} q) \sin(\omega t)] \quad (55)$$

Here it has been assumed that  $H_x = 0$  and  $H_y = H_{rf} \sin(\omega t)$ .

Using material parameters measured in this laboratory on sample 3-18-16 (see table 5), numerical solutions were obtained for Eqn. (55). A typical solution is shown in Fig. 22.

Based on the numerical solutions, analytic solutions to equation 53 were sought. If  $H_z = 0$ ,  $\dot{\psi} = -\frac{\alpha}{\Delta} \dot{q}$  implying that  $\psi = -\frac{\alpha}{\Delta} q$ . From the numerical solutions it is seen that  $\frac{\alpha}{\Delta} q$  is small enough that  $\sin \psi = \psi$  and  $\cos \psi = 1$ . Thus, Eqn. (53) becomes

TABLE 5

Material parameters of sample 3-18-16

$4 M$ - 259 G	saturation magnetization
$H_u$ - 1164 Oe	uniaxial anisotropy field
$A$ - $3.7 \times 10^{-2}$ erg/cm	exchange constant
$= 1.76 \times 10^7$ He/Oe	gyromagnetic ratio
$h$ - $4.1 \mu\text{m}$	film thickness
$l$ - $.50 \mu\text{m}$	characteristic length
$\alpha$ - $3.2 \times 10^{-2}$	Gilbert damping coefficient
$P_0$ - $8.33 \mu\text{m}$	zero field stripe period
$H$ - 95 Oe	cubic anisotropy field

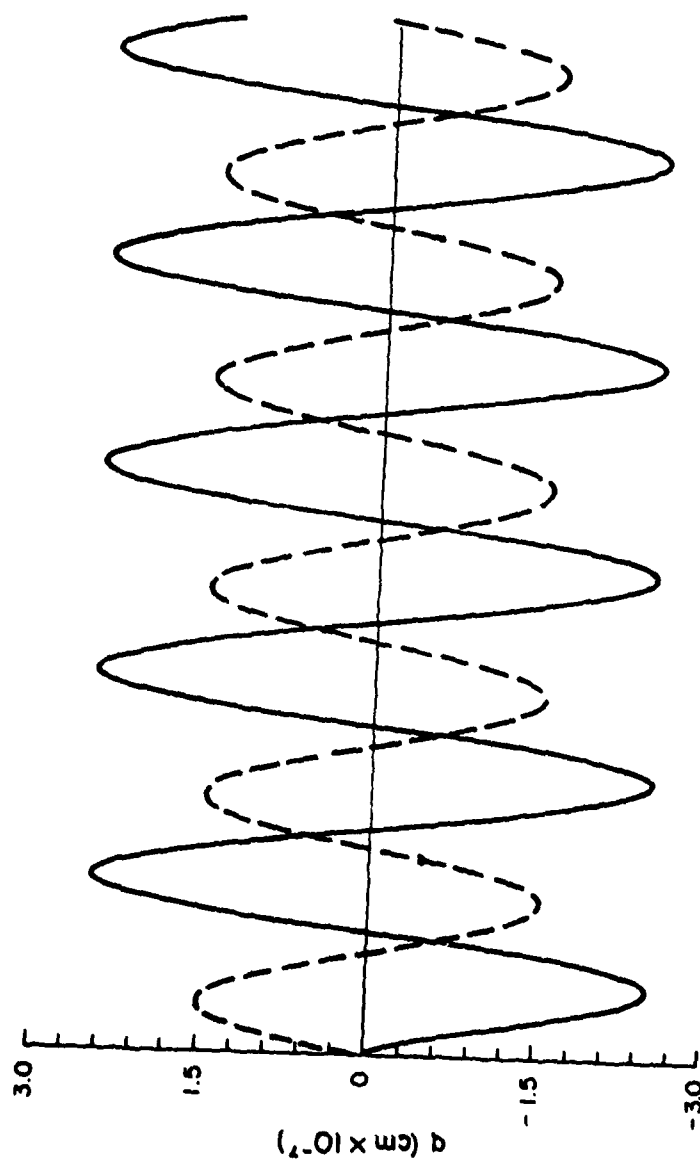


Fig. 22 Numerical solution for domain wall position as a function of time .  
Closed line shows time dependence of inplane RF magnetic field to  
show the phase relationship between drive field and wall motion.

$$(1+\alpha^2)\dot{q} = -4\pi M_Y \alpha q - \frac{\pi Y}{2} (H_X \alpha q + \Delta H_Y) \quad (56)$$

Solutions to Eqn. (56) can be found for the special cases  $H_X = 0$  and  $H_Y = 0$ . For the case  $H_X = 0$  and  $H_Y = H_{rf} \sin \omega t$  the solution is

$$q(t) = \frac{\pi \Delta H_{rf}}{2\omega \left[ \left( \frac{4\pi M_Y \alpha}{\omega} \right)^2 + (1+\alpha^2) \right]^{1/2}} \sin(\omega t + \phi) \quad (57)$$

$$\tan \phi = \frac{-\omega(1+\alpha^2)}{4\pi M_Y \alpha}$$

For the case  $H_Y = 0$  and  $H_X = H_{rf} \sin \omega t$  the solution is

$$q(t) = q(0) e^{\frac{-4\pi M_Y \alpha}{1+\alpha^2} t} e^{\frac{\pi Y H_{rf} \alpha \cos \omega t}{2\omega(1+\alpha^2)}} \quad (58)$$

Eqn. (57) represents an oscillatory motion of the domain wall, with a phase lag between the wall motion and the driving field. The amplitude of the oscillations is a complicated function of frequency and varies linearly with the magnitude of the drive field. Eqn. (58), on the other hand, represents an exponential decay of wall displacement modulated by a complicated oscillatory factor at the frequency of the drive field. For typical materials, the decay constant is on the order of  $10^8 \text{ sec}^{-1}$ , so that compared to the steady state behavior of Eqn. (57) this solution is only a transient and need not be considered in most cases.

Consider now the case where  $H_X = 0$  and  $H_Y = 0$  but both have the time dependence  $\sin \omega t$ . Then Eqn. (56) becomes

$$\dot{q} + (A + B \sin \omega t)q = C \sin \omega t \quad (59)$$

where

$$\begin{aligned} A &= \frac{4\pi M_Y \alpha}{1+\alpha^2} \\ B &= \frac{\pi Y H_X}{2} \frac{\alpha}{1+\alpha^2} \\ C &= \frac{-\pi H_Y \Delta}{2(1+\alpha^2)} \end{aligned} \quad (60)$$

Assume a solution of the form

$$q(t) = u(t)q_0(t), \quad (61)$$

where  $q_0(t)$  satisfies

$$\dot{q}_0 + (A + B\sin\omega t)q_0 = 0. \quad (62)$$

It can easily be shown that the solution to Eqn. (62) is

$$q_0(t) = q_0(0)e^{(At + \frac{B}{\omega} \cos \omega t)} \quad (63)$$

Using this fact, a differential equation for  $u(t)$  is found to be

$$\dot{u} = \frac{C \sin \omega t}{q_0(0)} e^{-At} e^{B/\omega \cos \omega t} \quad (64)$$

whose solution is

$$u(t) = \frac{C}{q_0(0)} e^{-At} e^{B/\omega \cos \omega t} \sin \omega t \, dt \quad (65)$$

Now, consider the case  $H_x = H_y = 0$ ,  $H = H\sin\omega t$ . In this case, Eqn. (53) becomes

$$\begin{aligned} \Delta^{-1} \dot{q} &= 2\pi M Y \sin 2\Psi + \alpha \dot{\Psi} \\ \dot{\Psi} &= \gamma H \sin \omega t - \frac{\alpha}{\Delta} \dot{q} \end{aligned} \quad (66)$$

The two parts of Eqn. (66) can be decoupled, and making a small angle approximation for  $\psi$ , the resulting equation is

$$(1+\alpha^2)\ddot{\psi} + 4\pi M_Y \alpha \dot{\psi} = YH \sin \omega t \quad (67)$$

The solution to Eqn. (67) is

$$\psi(t) = \psi_0 e^{-at} + \frac{b}{(a^2 + \omega^2)} \sin(\omega t + \phi) \quad (68)$$

where

$$\begin{aligned} a &= \frac{4\pi M_Y}{1+\alpha^2} \\ b &= \frac{YH}{1+\alpha^2} \\ \tan \phi &= \frac{-\omega}{a} = \frac{-\omega(1+\alpha^2)}{4\pi M_Y} \end{aligned} \quad (69)$$

and  $\psi_0$  is a constant determined by the value of  $\psi$  at  $t = 0$ . Inserting this solution into Eqn. (66) gives a differential equation for  $q$ . This equation includes terms proportional to  $e^{-at}$ . Since only steady state solutions can give rise to a long duration power absorption, these terms can be ignored. The equation for  $q$  then becomes

$$\dot{q} = \left(\frac{4\pi M_Y \Delta}{2}\right) \left(\frac{2b}{(a^2 + \omega^2)^{1/2}}\right) \sin(\omega t + \phi) + \frac{b\alpha\omega}{(a^2 + \omega^2)^{1/2}} \cos(\omega t + \phi) \quad (70)$$

The solution to Eqn. (70) is

$$q(t) = C \sin(\omega t + \phi + \phi') + D \quad (71)$$

where

$$C = \omega^{-1} \left[ \frac{(4\pi M_Y \Delta b)^2 + (b\alpha\omega)^2}{a^2 + \omega^2} \right]^{1/2} \quad (72)$$

and

$$\tan \phi' = \frac{-4\pi M_Y \Delta}{\omega \alpha}$$

and the value of  $D$  is determined by the wall displacement when  $\sin \omega t = 0$ .

In order to calculate the power absorbed by the wall motion, it is necessary to know the force acting on the wall. According to Slonczewski<sup>(22)</sup>, the wall momentum is

$$p = \frac{2M}{Y} \dot{\psi} \quad (73)$$

and assuming that  $H_z = 0$ , the force acting on the wall is

$$F = \dot{p} = \frac{2M}{Y} \ddot{\psi} = \frac{-2M\alpha}{Y\Delta} \dot{q} \quad (74)$$

so that the work done in moving the wall is

$$dw = \frac{-2M\alpha}{Y\Delta} \dot{q} dq \quad (75)$$

The power absorbed is then

$$P = \frac{dw}{dt} = \frac{-2M\alpha}{Y\Delta} \frac{d}{dt} (q\dot{q}) \quad (76)$$

Using the solution given by Eqn. (57), this is

$$\frac{4\pi M Y \pi \Delta \alpha H r f^2}{4[(\frac{4\pi M Y \alpha}{\omega})^2 + (1+\alpha^2)^2]} \cos^2(\omega t + \phi) - \sin^2(\omega t + \phi) \quad (77)$$

A plot of the amplitude of Eqn. (77), using the material parameters of sample 3-18-16, is shown in Fig. 23. A plot of this same relationship, using material parameters of sample TI330, along with data taken on TI330, is shown in Fig. 24. Agreement between experiment and theory seems to be reasonable.

Note, too, that since  $H_{rf} \propto \sqrt{P_{in}}$ , where  $P_{in}$  is the power input to the coil,  $P \propto P_{in}$ , in good agreement with the data of Fig. .

Thus, this theory seems to provide an adequate explanation of the data, and in particular provides a mechanism whereby an inplane rf



Fig. 23 Power absorption in frequency sample 3-18-16

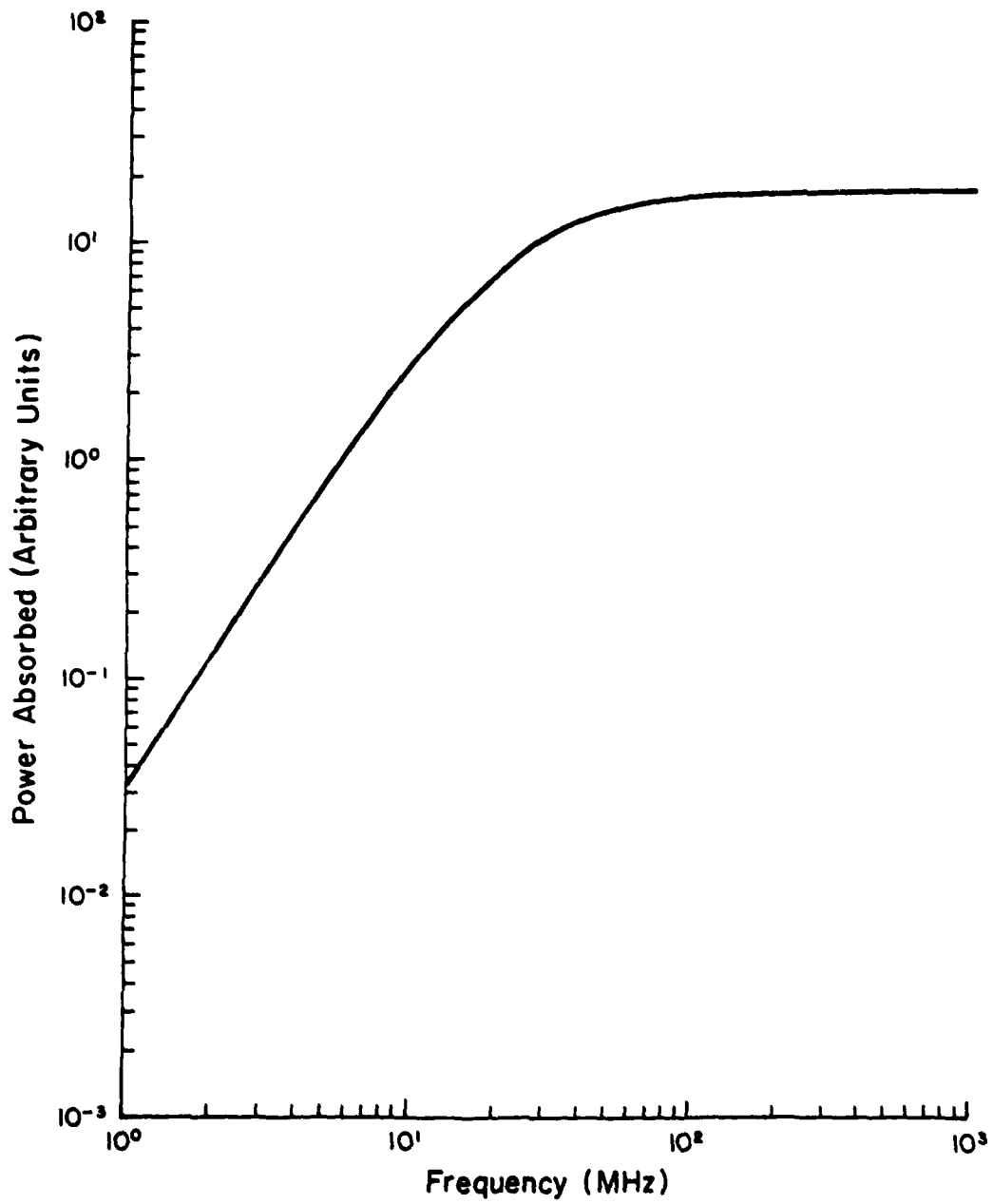
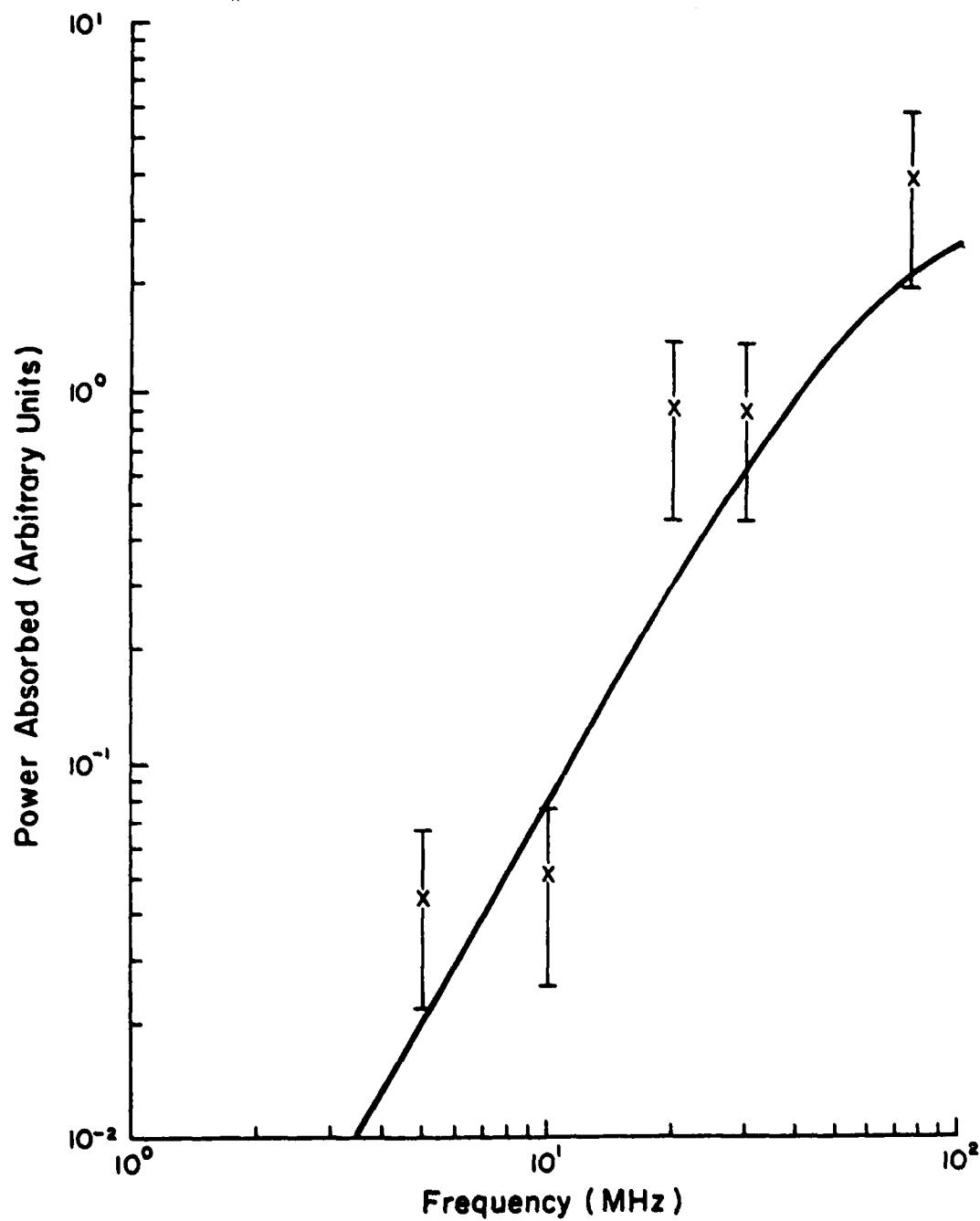


Fig. 24 Power absorption vs. frequency sample TI 330  
Theory curve is least squared fit to data points.



magnetic field can drive domain wall motion. More experimental work needs to be done to evaluate the qualitative and quantitative predictions of this theory, and the modified spectrometer described in the previous section will be capable of obtaining the necessary data.

## SECTION II

### Testing Program

#### A. Overlap Pattern Verification

Perhaps the largest class of visual pattern recognition problems involve the identification of objects whose presentation is either different in time or whose context is variable. For example the recognition of aircraft (23) involves the identification of an object whose orientation and size is constantly changing. Face identification (24,25) has similar problems plus variations caused by changes in facial expression, makeup, hair style, etc. Many more examples could be cited all of which require object identification in a changing environment (26). There appear to be few problems of real interest which involve patterns fixed in space and time. Certainly little appears in the open literature concerning such problems. The advent of bubble memories (27) however has created interest in just such a problem.

The simplicity and low number of masking operations required in the construction of a bubble memory, make possible the development of extremely large memories of the order of  $10^9$  to  $12^{12}$  bits (28). Because of the immense size involved, exhaustive testing of each memory device becomes excessive. Consider, for example, a  $10^9$  bit memory running at 500 k bits/sec. Such a memory requires 2000 sec. or 3.3 hrs. to access every bit once. Thus a complete memory test, including tests for pattern errors, could take several days. Obviously some gross pretesting is necessary to reduce the number of devices which must be exhaustively tested. Clearly if a fault free magnetic substrate (garnet, for example) and a fault free permalloy overlay and aluminized conduction paths exist, then the probability that a memory device works is extremely high. This sorting on the basis of these two factors should reduce the overall testing time of

the memory elements. Further, in order to increase yield rates, manufacturers currently allow some overlay faults to exist if these faults can be isolated and removed from service without affecting the rest of memory (29). Thus any overlay faults detected should be marked so that specific tests can be performed to determine their effect on the rest of the device. The purpose of this paper, therefore, is to describe the experimental, optical test procedure which has been shown feasible in checking overlay patterns for faults in four micron bubble, bubble memories.

Basically the problem involves detecting differences between two fixed geometry patterns. One of these patterns, the fault free one, is taken as the authority and the other is compared to it in some appropriate fashion. Such a procedure is generally termed template matching (30). The major difficulty with any pattern recognition problem is the selection of the features to be used in making the comparisons. It is tempting in problems where the geometry is absolutely fixed to use a pattern description language (31,32) to define a correct pattern and then compare the derived description of the sample to that of the authority. Unfortunately, deriving a description of a pattern is generally a time consuming proposition. It would seem, therefore that statistical recognition techniques (33,34), which generally require less time for feature extraction than do syntactic techniques (35) would be the procedure of choice.

The selection of features to be used in a geometrical or statistical approach to pattern recognition is perhaps the single most important factor in the success of recognition. Unfortunately, there is little in the way of a general theory to help in the selection of these features. However, for the problem being considered here three factors are important:

- 1) the features should be rapidly computable
- 2) they should be capable of isolating the location of a fault in the field of view and not merely identify that a fault exists, and
- 3) only a small number of features should be required.

The first requirement is due to the very large number of views necessary to cover a large scale bubble memory chip with adequate resolution. More will be said about this later. The second requirement is necessary so that faults which affect only portions of a memory chip can be isolated and removed from service in some way. The last requirement is necessary so that computer memory space is kept to some reasonable value.

Autocorrelation coefficients (36), Fourier transform coefficients (37) and moment invariants (38) have all been used with varying degrees of success in optical pattern recognition problems. Certainly criteria 1 and 3 above are satisfied for these features. Unfortunately, all of these features tend to represent the image in a rather "global" way, that is, little or no information is obtained about local characteristics. Histograms, however, appear to meet all three requirements and therefore were the features selected for this problem.

The images used are binary, black-white images which are mapped onto a 128 x 128 bit binary array. Two sets of histograms are obtained from this array; horizontal and vertical. The  $i$ th element of the horizontal histogram represents the number of white cells on row  $i$  of the image array. Similarly for the vertical histogram components. If it is assumed that only a single "blob-like" fault occurs within the field of view then a comparison of the horizontal and vertical histograms with those of the authority should localize the fault in the image plane.

## EXPERIMENTAL SYSTEM

Generally large bubble memory devices are integrated on large (perhaps a few square inches) substrates. It is obvious then, that a very large number of views will be required to cover the device with adequate resolution. For example a  $10^6$  bit memory with 16 micron elements on a one square inch substrate would require roughly 10,000 separate nonoverlapping views to cover the entire surface.\* Positioning the device under a microscope with the accuracy necessary is, of course, an extremely difficult problem. However, systems such as the Leitz Step and Repeat camera (39), which is capable of positioning to within  $\pm 0.2$  microns might be capable of handling the problem. More will be said about this in section B below.

Assuming that the positioning problem is solvable, the recognition task becomes one of acquiring an image, preprocessing to clean and smooth it, extract the histogram features, and finally determine if faults occur. The images used in this work were obtained by a Zeiss model microscope from an experimental bubble memory device of approximately 24,000 bits. Figure 25 shows one such photograph. These photographs were next blown up to an 8x10 size and digitized by a TV system connected to a DEC PDP-9 computer (41,42). The resulting binary images were then smoothed in an 128 x 128 binary image array processor (43) also connected to this computer. Figure 26 shows the resulting control image used for the experiments described in what follows.

Two experiments were carried out. The purpose of the first was to determine the efficacy of the histogram features for identification and isolation of overlay pattern faults. The second experiment was intended to determine the effects of positioning error on fault detection. In the training phase of experiment one, the control image

---

\*This assumes an 128 x 128 image and that two pixels per 4 micron line width are required for adequate resolution.

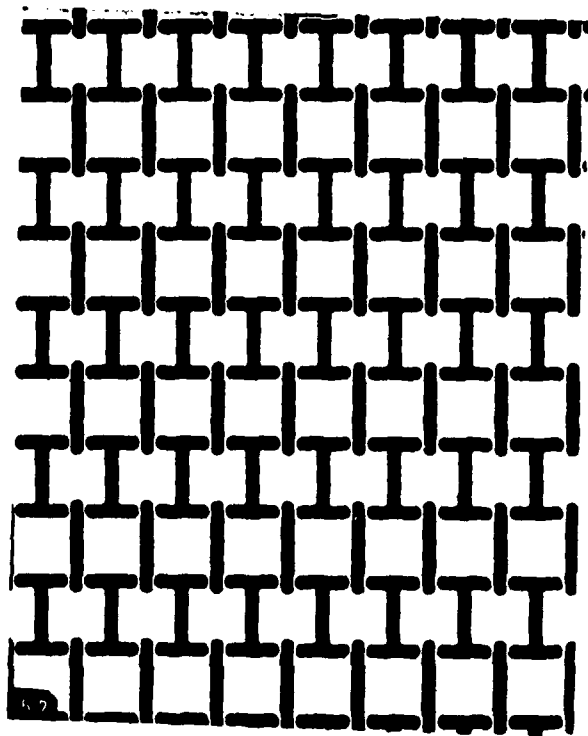


Fig. 25 Original Overlay Pattern.



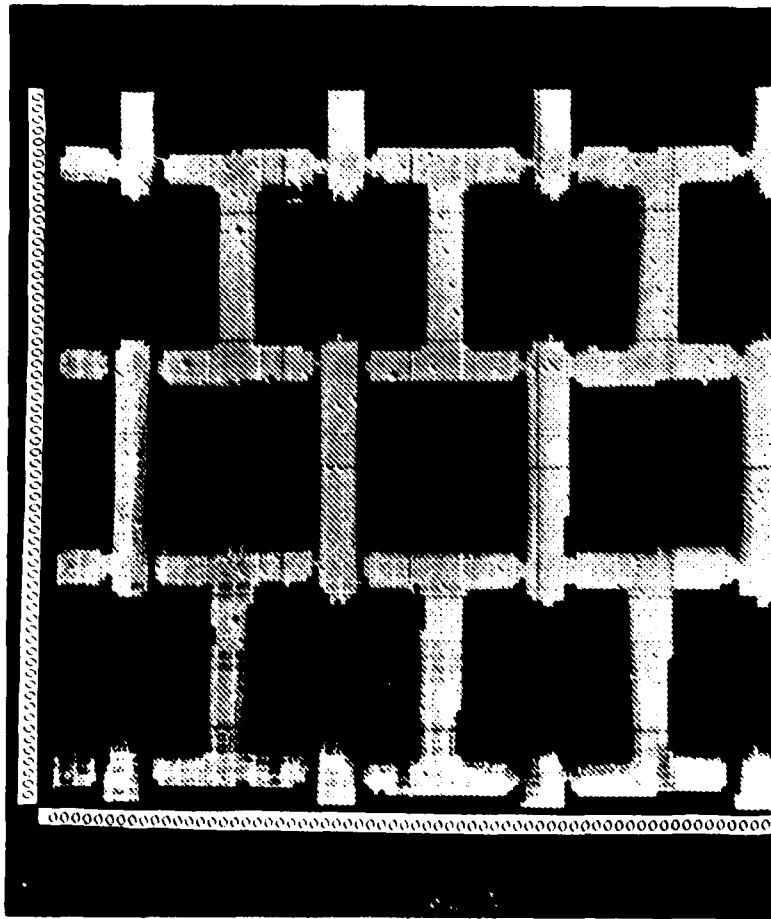


Fig. 26 Control Image.

was input to the system 10 successive times without motion and the horizontal and vertical 128 number histograms were computed at each trial. The average value and standard deviation were then computed for each of the 256 histogram components. The resulting average histograms with their supplementary standard deviation information, was then used as the authority for the recognition phase of the experiment. This averaging process was carried out to reduce the effects of camera chain noise on the results.

In the recognition phase of the first experiment overlay pattern faults were simulated by either adding to the pattern or occluding portions of the pattern. This was done by placing irregularly shaped white and black pieces of paper on the input photograph. Two sizes were used for these faults; a large error, roughly the size of the top of one of the T's, and a small error, about the width of a bar in the image. The modified image was then input to the system and the histograms computed. For each component of the histogram a binary classification number was computed as

$$C_i = \begin{cases} 1 & \text{if } \frac{h_i - \bar{H}_i}{SD_i} \geq T \\ 0 & \text{otherwise} \end{cases} \quad (78)$$

where  $h_i$  is the  $i$ th component of the sample histogram,  $\bar{H}_i$  is the mean of the authority histogram component  $i$ ,  $SD_i$  is the standard deviation of the authority histogram component and  $T$  is an arbitrarily set threshold. In order to avoid problems of quantization noise which occurs when a scan line is on the edge of image element, a second classification number  $D_i$  was introduced as

$$D_i = \begin{cases} 1 & \text{if } C_i = C_{i+1} = 1 \text{ or } C_{i-1} = C_i = 1 \\ 0 & \text{otherwise} \end{cases} \quad (79)$$

$$i = 1, 2, \dots, 255$$

where the first 128 components correspond to the horizontal histogram and the last 128 correspond to the vertical. Figures 27, 28, 29, and 30 show the results of this experiment. In these figures the  $D_i$  is plotted along the edge of the picture and used  $T=6$  standard deviations. The important thing to observe is that, indeed, the faults in the overlay patterns were detected and furthermore were located by the positioning of the  $D_i$  values.

In order to determine the effects of positioning error on the recognition accuracy a second experiment was carried out. In the training phase of this experiment the control image was allowed to vary by  $\pm 1/2$  pattern bar width in both the horizontal and vertical directions. The authority histograms were then computed on the basis of two samples taken at each of the eight possible off center positions plus the centered image. These 18 samples were used to compute the control histogram component averages and standard deviations.

Equations 78 and 79 were again used in the recognition phase. The additive and subtractive faults were simulated as before and are shown in Figures 31 through 38. The  $D_i$  plotted in Figures 31 through 34 used a threshold,  $T$ , of 6 as in the first experiment and those of Figures 35 through 38 used a threshold of 2. The additive faults shown in Figures 31 and 32 are, indeed, marked by the  $D_i$ . However, the fault in Figure 32 is detected only in the vertical histogram and not the horizontal. Figure 33 shows a large subtractive fault in the horizontal, but not the vertical, histogram. The subtractive fault of Figure 34 is undetected at threshold level 6.

Figures 35 through 38, however, which represent the same faults but use a threshold of 2, do show all faults as being identified.

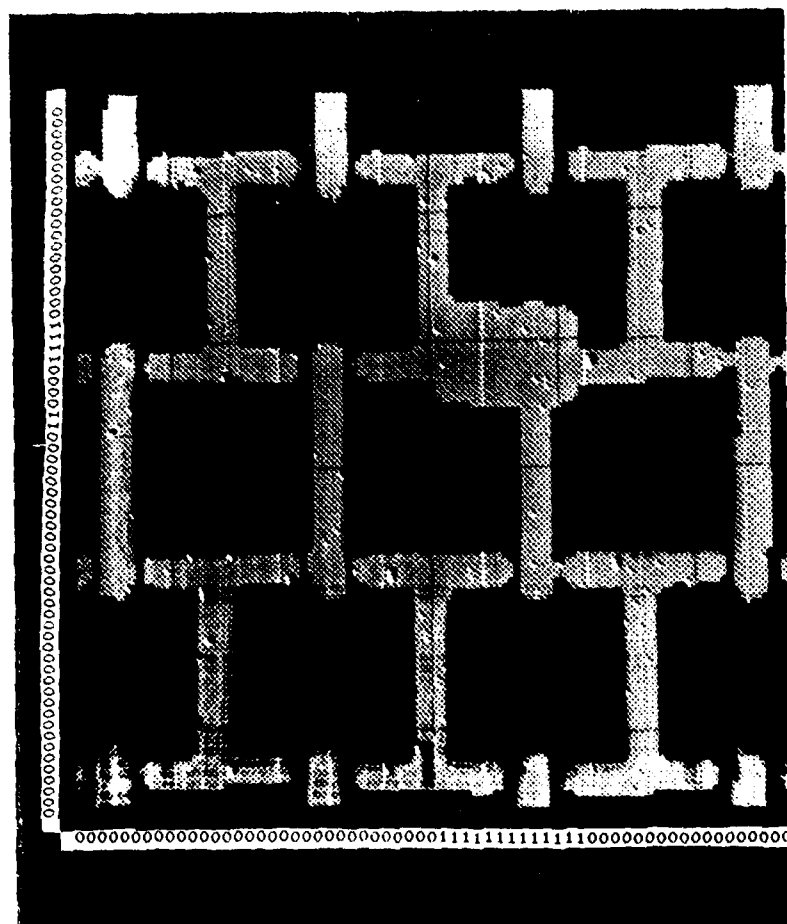


Fig. 27. Large Additive fault.

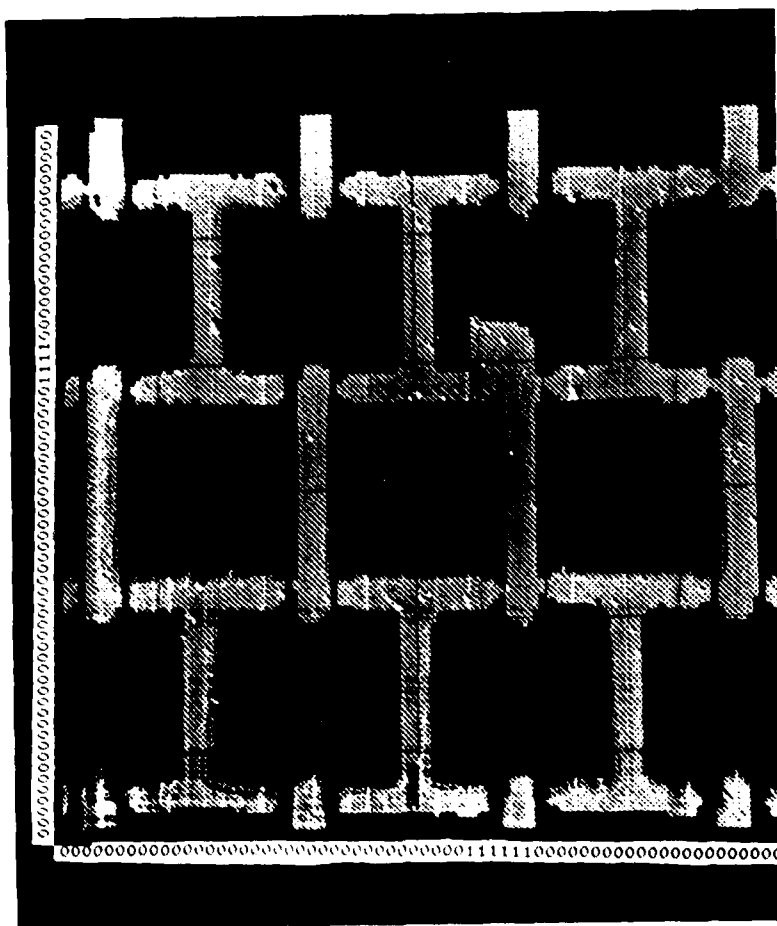


Fig. 20. Additive fault.

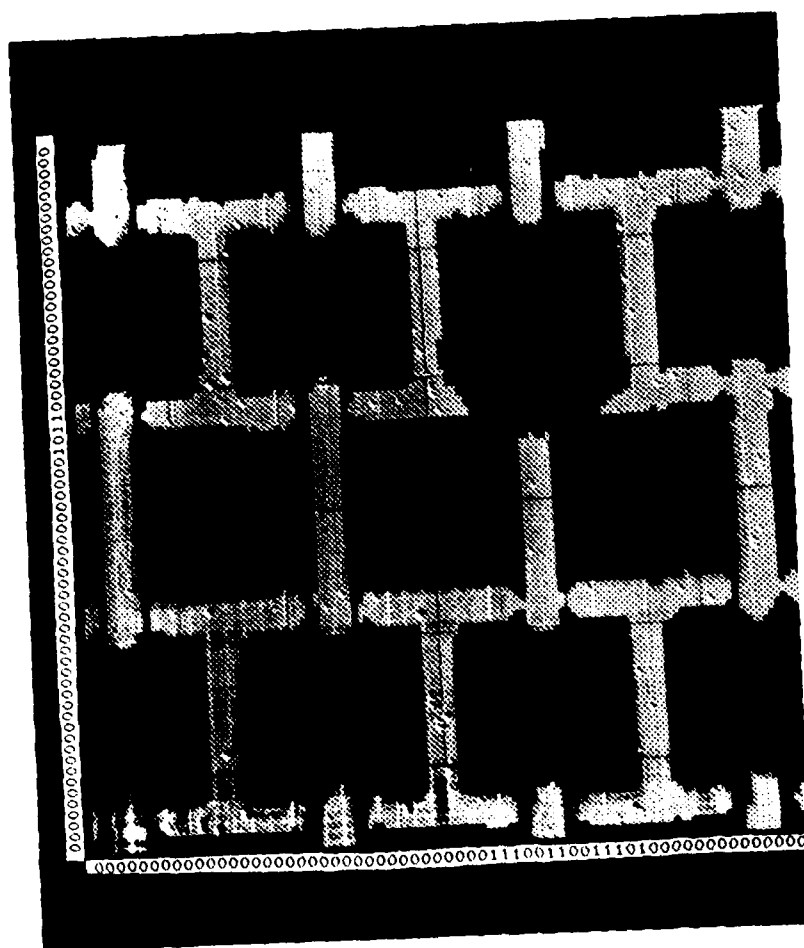


Fig. 29. Large Subtractive Fault.

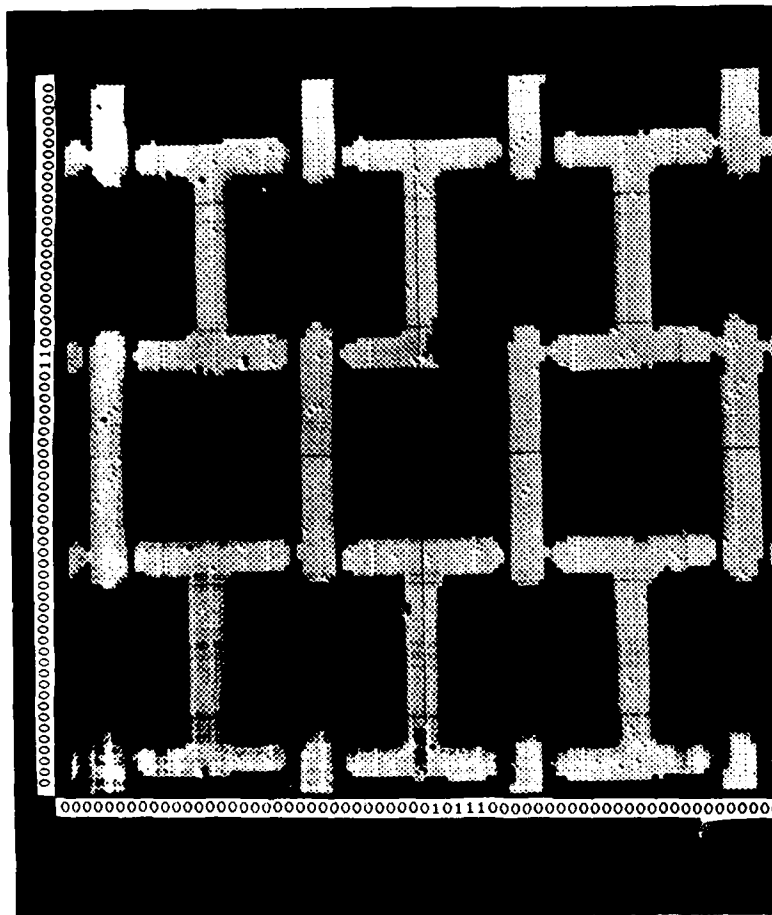


Fig. 30 Small Subtractive Fault.

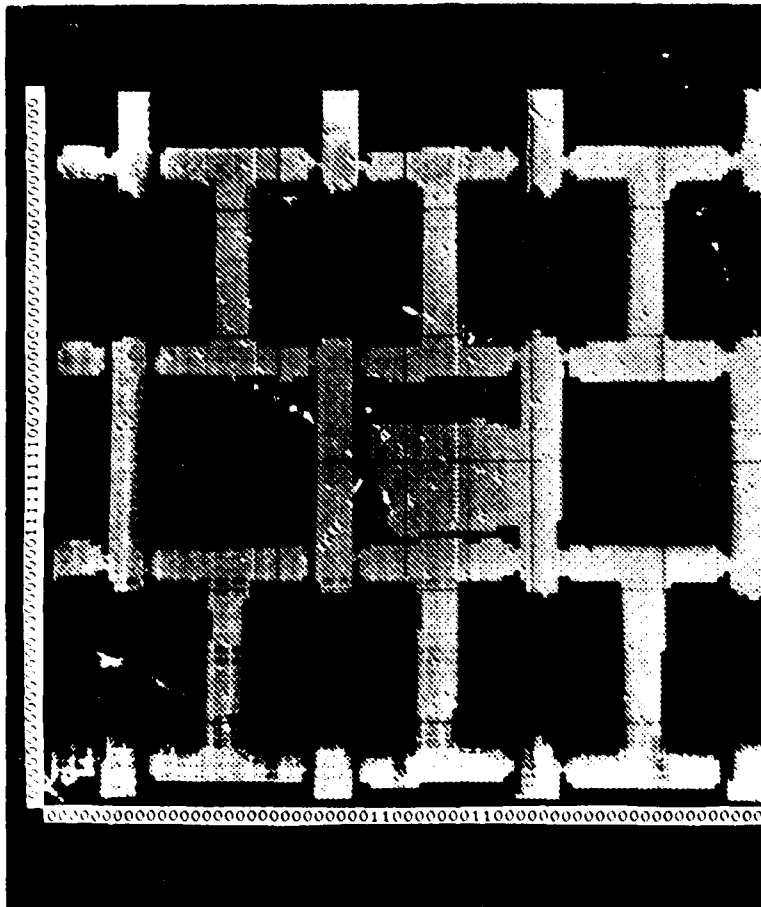


Fig. 31 Large Additive Fault, 1 b.



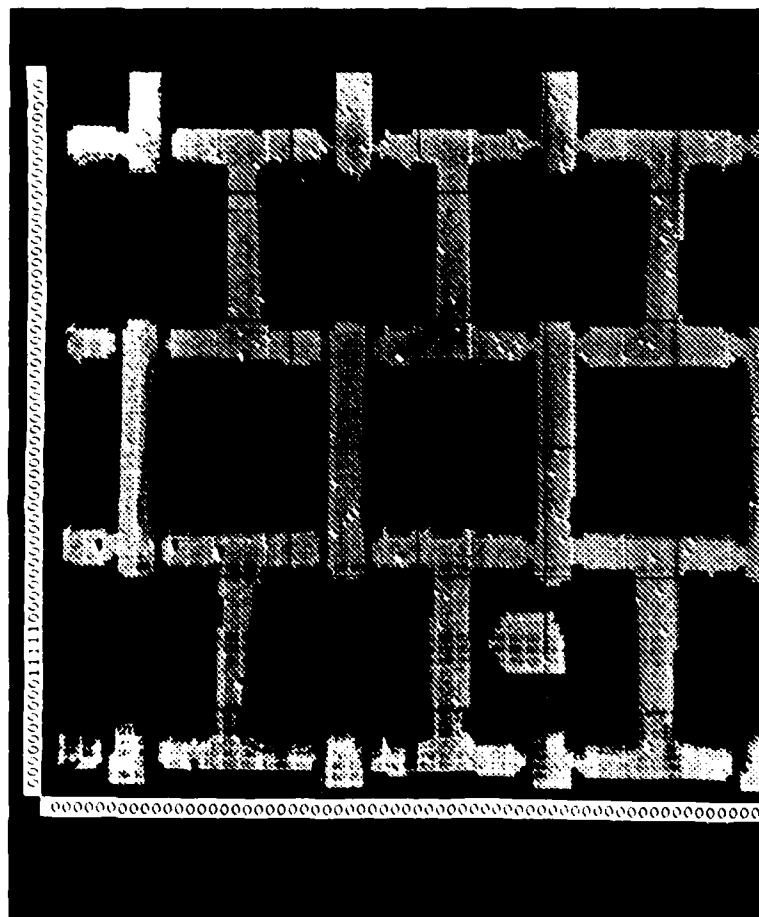


Fig. 32 Small Additive Fault, T 6.

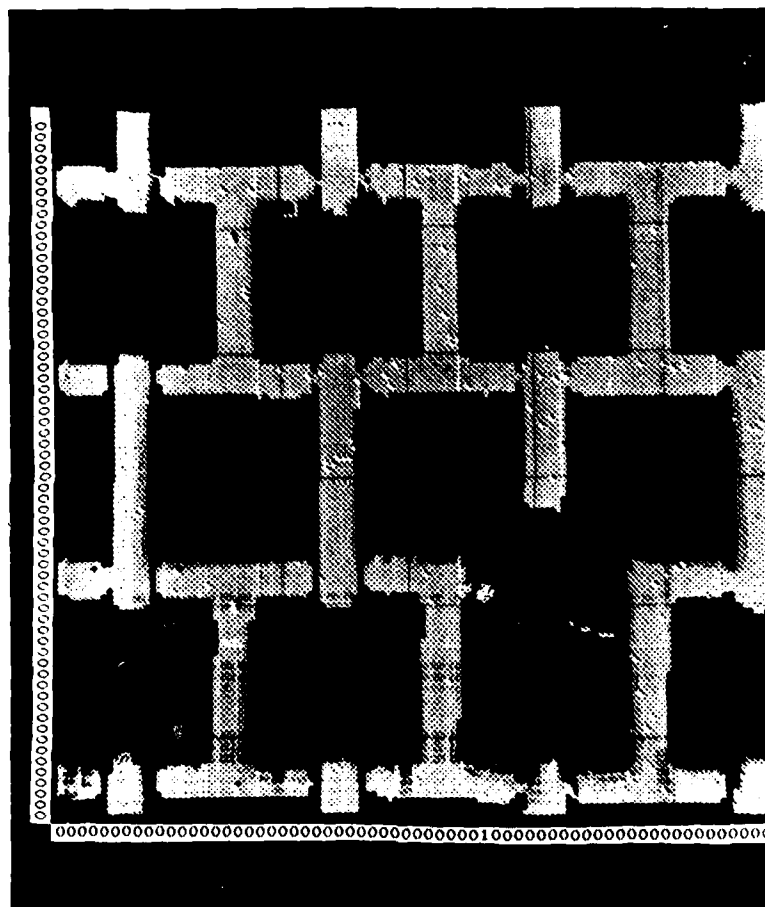


Fig. 33 Large Subtractive Fault, T-6.

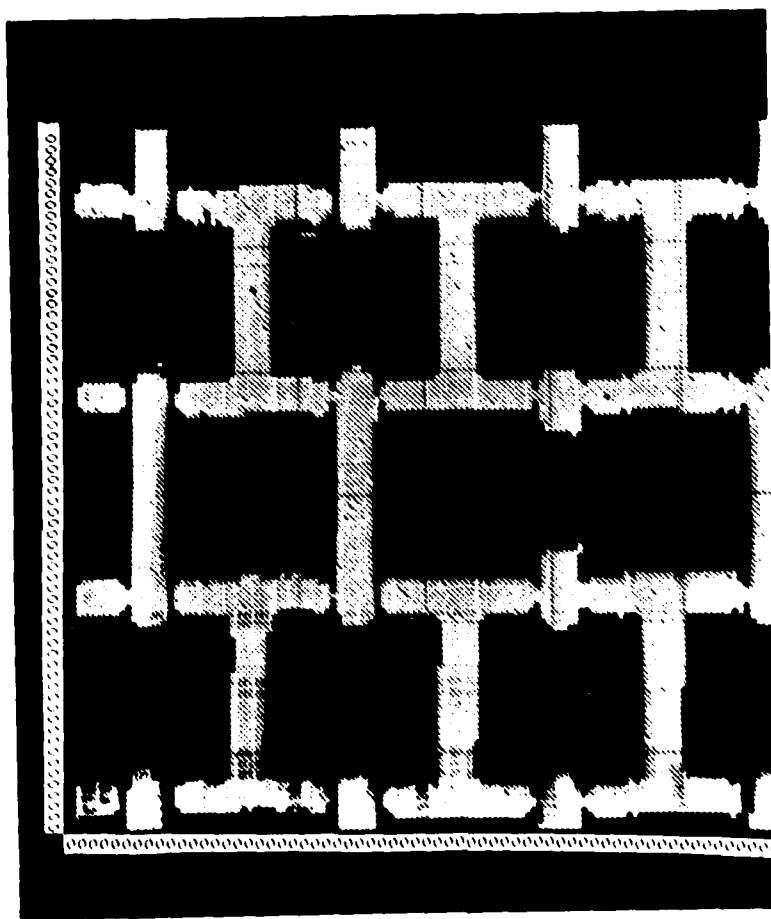


Fig. 34 Small Subtractive Fault, 16.

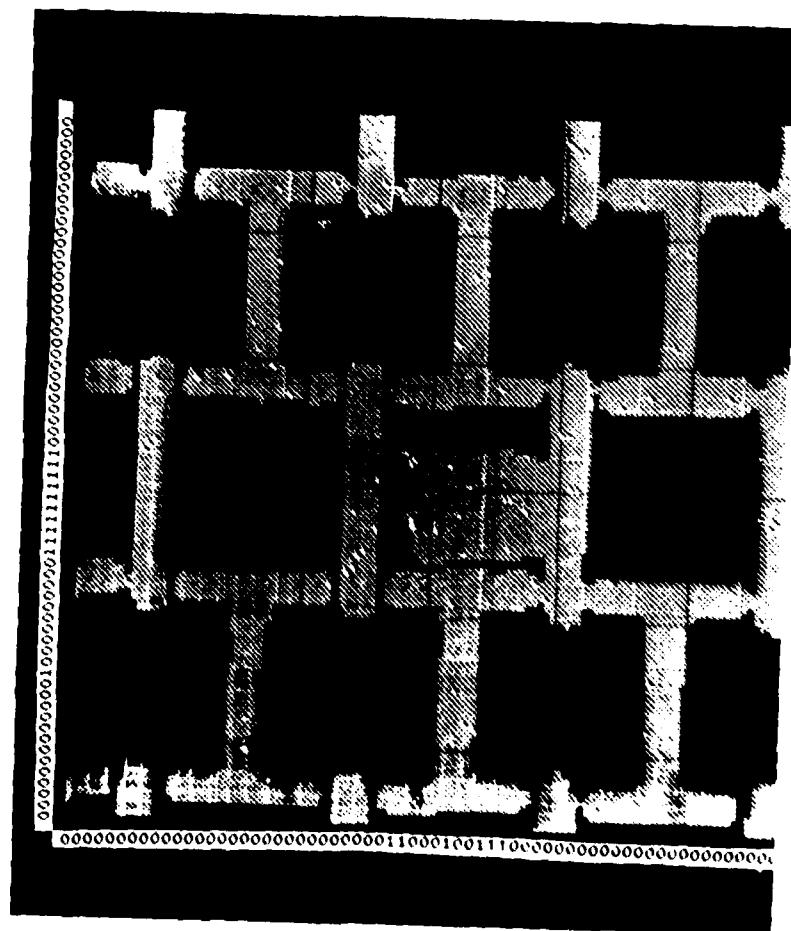


Fig. 35 Large Additive fault, T 6.

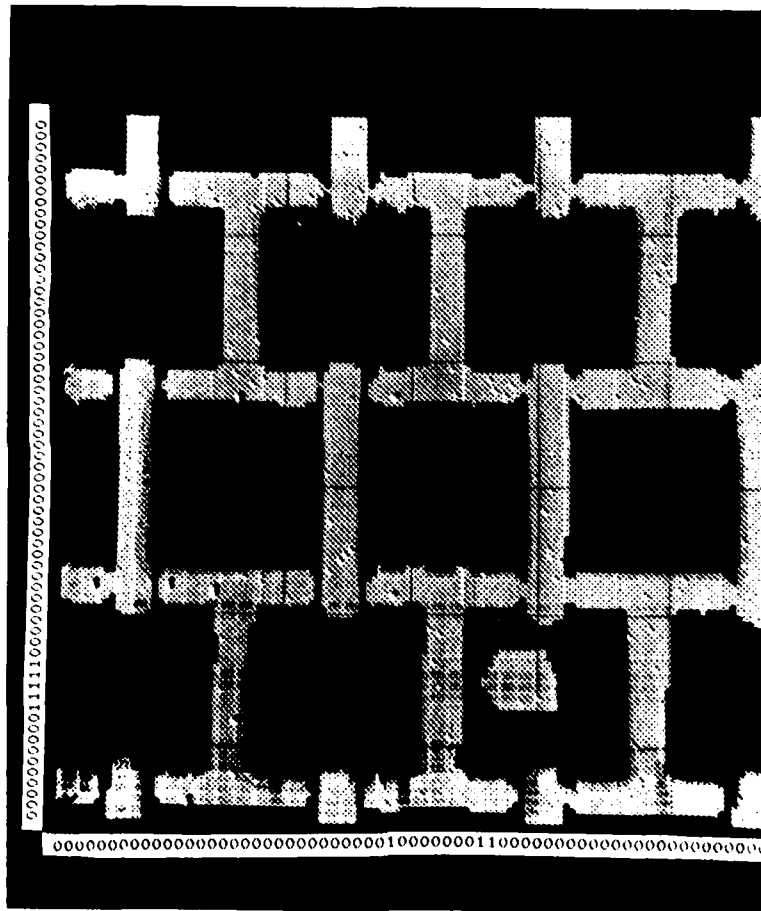


Fig. 36 Small Additive Fault, 1.2.

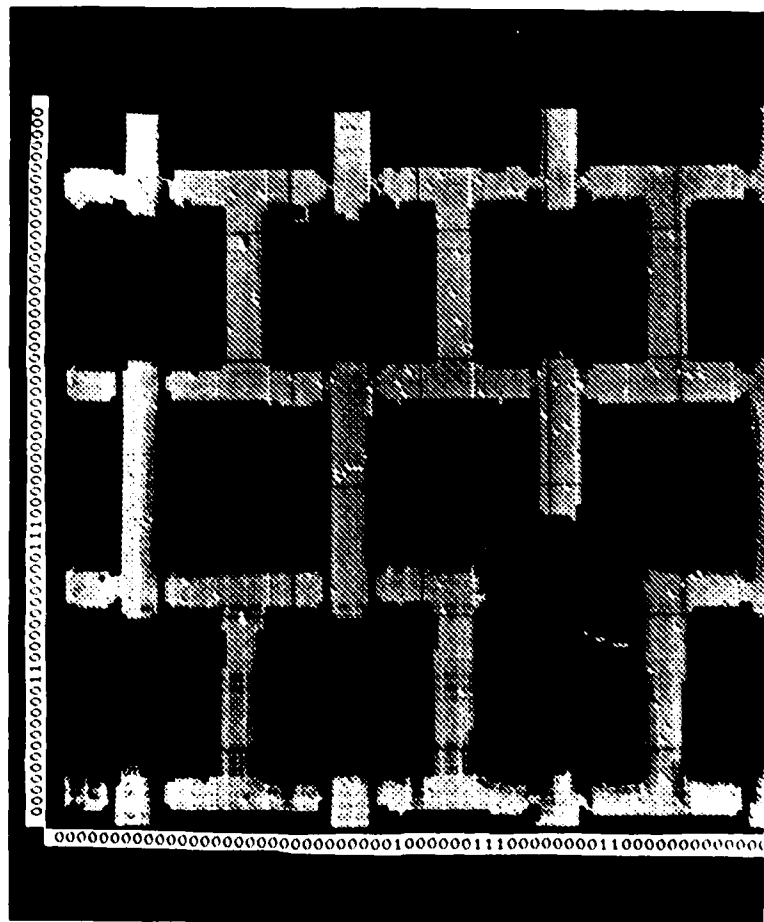


Fig. 37 Large Subtractive Fault, 1 2.

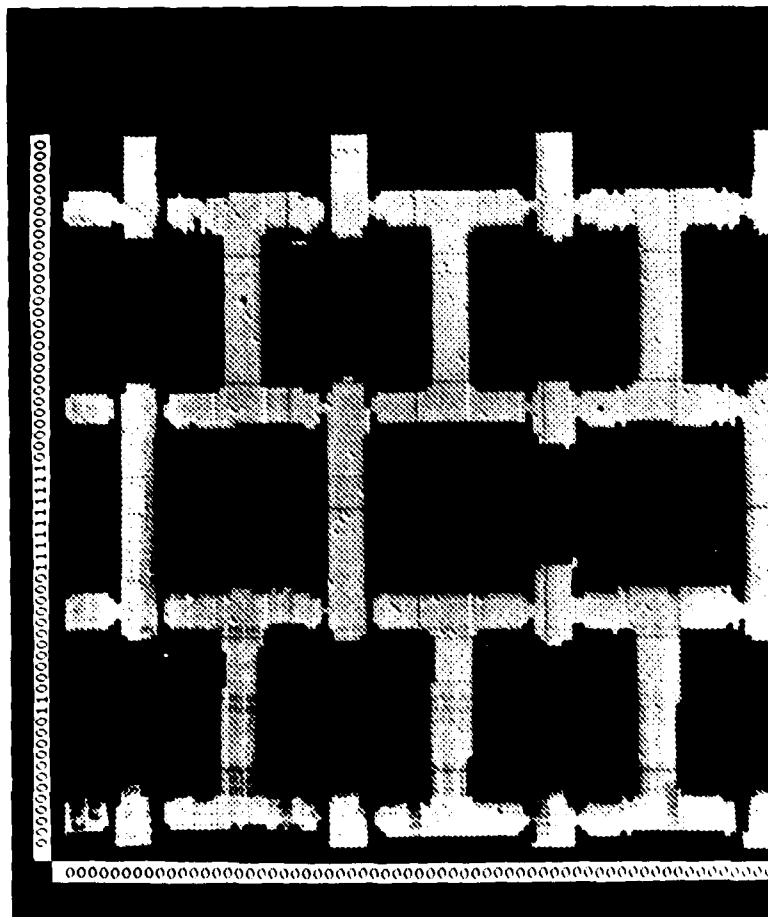


Fig. 38 Small Subtractive Fault, 1 2.

However, some false alarms start to appear. The obvious implication is that there is a coupling between positional variation of the device, the optimum threshold for detecting the faults, and the rate of false alarms.

## CONCLUSIONS

It is obviously impossible to draw any major conclusions from the small sample size given here. However, it is equally as clear that the histograms do appear to mark the faults, both additive and subtractive, at least for the samples taken. Furthermore, it would seem that positioning variations of up to  $1/2$  bar width are tolerable. Thus the use of histogram features for detection of faults in fixed geometry problems would appear to be feasible.

### B. Positioning Problem

As stated above, the general approach being taken in the verification of the overlay pattern is to scan the overlay in several steps each time comparing the actual image with a corresponding perfect image. Errors will show up as differences in the comparison. Since the overlay pattern is quite large, it will, in general, be necessary to move the pattern relative to the optical axis.

Because of this some mechanical positioning mechanism is required to move the overlay array relative to the sensor with at least two mutually perpendicular degrees of freedom. (Assumes angular orientation already established). The requirements and constraints applicable to each of these degrees of freedom are nearly identical so it will suffice to discuss only one.

It is generally true that mechanical positioning mechanisms are



frought with numerous inherent nonlinear characteristics which result in position errors which are rarely repeatable from one trial to the next. Dead-zone due to gear train backlash in the presence of friction probably constitutes the major source of error. The extent to which nonlinear effects can be masked is a function of the type of servomechanism used.

There are two basic types of electrically actuated positioners. First, the open loop or open cycle type. Typically, these consist of a step motor driving a load through a low backlash gear train. In such a drive the accuracy of positioning of the load is determined by the dynamic and static characteristics of the step motor and by the backlash and frictional properties of the gear train as well as the friction and inertia of the load.

A typical step motor indexes 200 steps per revolution with non-accumulative angular position error. However, the static error (a quantity not usually specified by manufacturers) at a given step position must be considered. The torque available to the load is approximately a linear function of angular position deviation about the desired position, is

$$T \cong K(\theta - \frac{360^\circ}{200} n)$$

where  $\theta$  is the actual angular position in degrees

$n$  is the increment number for a 200 step per revolution motor

$K$  is the steady state torque constant

The magnitude of  $K$  is a function of the size of the motor and the magnitude of the excitation current.

The dynamic characteristics of step motors must also be considered. An unloaded step motor is governed by an underdamped second order characteristic equation, i.e., its angular shaft position leaves a steady-state, approaches and overshoots the new desired position, then oscillates with an exponentially damped amplitude about the new

steady state position and finally stops. A mechanical load in the shaft alters the overshoot, ringing frequency and rate of exponential damping. Nearly always an unrealistically large amount of external viscous damping is required to eliminate overshooting. (The exception is that one can decrease overshoot for a given load by decreasing motor current. The sacrifice is usually intolerable since  $K$  and steady state position error increase with decreasing excitation current.) In some instances, it is possible to use some type of Geneva mechanism to mask the effects of overshoot and ringing.

Thus a very careful mechanical design must be incorporated in step motor-driven open-loop designs to maintain error at an acceptable level.

The second basic type of electrically actuated positoner is a closed-loop type in which a motor (not a step motor) overcomes friction and moves through the backlash deadzone until the load reaches the desired position. At such a time the motor exerts whatever torque is necessary to maintain the load at the desired position within a position error of  $\pm \epsilon$ . In this case however, given a type 1 servo controller, the magnitude of  $\epsilon$  is primarily a function of the resolution limits of the transducer sensing the position of the load. In the extreme case it is conceivable that one could use an optical defraction grating positon-sensing transducer, e.g., the Leite Step Repeat Camera in which a  $\pm .2\mu\text{m}$  position accuracy is specified. (The width of permalloy overlay bars in the sample available is approximately  $3\mu\text{m}$ ).

Obviously the closed-loop approach involves a higher degree of complexity and expense however, position accuracy and repeatability far exceed those of an open-loop configuration.

The following consists of a discussion of positioning accuracy requirements for two broad classes of patterns: a) those patterns which are repeated in both the  $x$  and  $y$  directions, and b) non-repeated

patterns consisting of isolated features or long narrow strips of features. It is also to be expected that positioning accuracy will be strongly influenced by the limitations of the pattern recognition technique used.

First, it should be recognized that a closed-loop positioner with an accuracy of  $\pm .2\mu\text{m}$  opens options not available with lower accuracy positioners. For example, no overlapping of scanning would be necessary, software search modes to locate a non-periodic feature would not be required, the position of the boundary of a repeated pattern would be precisely known. An attempt will be made to specify the extent to which lesser accuracies would be feasible.

The type of pattern imposing the least stringent positioning accuracy demands is one which is repeated or periodic in both X and Y. Such a pattern could be examined in successive narrow overlapping strips, each strip being divided into n overlapping subsections. The data collected from each subsection would be compared with idealized data from a model pattern. Obviously if there are p basic X-cycles and r basic Y-cycles in the mode, the portion of sensed data actually used must contain exactly p and r basic X and Y cycles respectively. There are two important conclusions from the foregoing. First, sensor deflection magnitude and rate must be extremely closely controlled since it is the scan velocity which bridges the gap between actual length and the apparent length of a scanned object. It is conceivable that a closed-loop scan control using an edge groticule sensed by the scanner as feedback would be required.

The second conclusion is that since only a portion of the data obtained from scanning a subsection of the overlay pattern can be used, the overlap of the scanned subsections must be determined from the dimensions of the unused portions of the subsection. Specifically, the distance between center of scanned subsections, D, must be

$$D < P \cdot \delta_x - 2\epsilon - \delta_x = (p-1) \delta_x - 2\epsilon$$

where  $\delta_x$  is the X dimension of a basic X-cycle

P is the number of basic X cycles in the model

$\pm\epsilon$  is the maximum position error.

From this inequality one can conclude that for a repeated pattern nearly any position error would be acceptable provided the increased processing time resulting from greater overlap could be tolerated.

As long as processed areas did not include the boundary of a periodic array, the scheme described appears to be viable. Special problems arise when boundaries are inevitably reached. A means would have to be developed for distinguishing between sensed data discrepancies from the ideal due to faulty patterns and that due to the scanning of a legitimately incomplete subsection.

Non-repeated portions of a pattern may pose more stringent positioning accuracy requirements than the repeated type. If relatively low positioning accuracy, i.e., error greater than one basic cycle were considered, some type of search mode would be required to locate an isolated narrow line of overlay patterns. The searching and subsequent processing of such a pattern would have to be capable of discriminating between erroneously deposited blobs and legitimate patterns.

Another type of problem will exist in the data collection process regardless of the pattern configuration. A given scan line will inevitably run along the black-white or 1-0 boundary of a section of overlay. The resulting raw data will be a somewhat random sequence of 1's and 0's. The question which must be addressed is, can such noise be successfully handles without excessive compromise or must provisions be made to make minute scan position corrections when such a situation is detected?

If the need to examine the basic cycles in the vicinity of the edge of a continuous array did not exist, and also if no non-periodic patterns required processing, positioning accuracies well within the capability of open loop step motor positioners could be used. However, since such patterns must be included the question remains: can sufficiently sophisticated pattern recognition techniques be incorporated to compensate for the rather gross position uncertainties of an open loop positioner, or must the positioner be made to be more sophisticated to eliminate position ambiguity?

Another requirement completely independent of the foregoing is that scan velocity must be sufficiently closely controlled to avoid time varying magnification errors.

Unfortunately, due to early termination of this contract, little experimental work was carried out to determine requirements on positioning accuracy. Some preliminary results have been presented in part A above and indicate the feasibility of the approach.

#### C. Optical Waveguide Work

Once the correctness of the overlay pattern is verified, dynamic testing of the chip is required. In order to speed this testing up it is necessary that multiple detection paths be present. As proposed here these paths are optical in nature and generally require that polarized light be coupled into the substrate region and then coupled out of this region after having the polarization shifted by Faraday Rotation due to any bubbles in the light path.

The experiments performed in the early months of the contract were directed toward coupling light into thin film waveguides by using gratings. This method was used to aid in the physical contact between the magnetic bubble memory chip to be tested and the integrated optic test circuit. Two different approaches were considered while

using gratings. Figure 39 shows the light coupling into the film from the air, while Figure 40 shows the second method of coupling the light from the substrate side. These two methods were evaluated by first, spinning on KTP positive photoresist at 300 RPM and contact printing a grating of .1 mil lines spaced 300 mil apart using standard photolithography procedures on a YIG film grown on a GGG substrate. Next the sample was placed in an experimental apparatus so that a HeNe laser could be directed toward the front as shown in Figure 39 and the back as shown in Figure 40. The intensity of the input was measured to be .78 mwatt while the maximized output was measured to be 0.34 mwatt for the front and .063 for the back. The output was maximized in each case by varying the angle of incident. Since coupling from the front has no mechanical advantage and the coupling efficiency is less than that of coupling from the back side, it leads to the conclusion that coupling from the back is a better approach. However 10% coupling efficiency is not good enough since the lost energy is scattered throughout the device and surrounding space. Another problem arose when the magnetic moment parallel to the surface was refracted in a localized area by applying an external magnet. When measuring the output the percentage change in the light level was too small to detect. From these results it was concluded that a different method of coupling light into the waveguide was needed.

By using rutile prisms which are highly birefringent a TM wave being decoupled from a thin film waveguide will be separated by  $20^{\circ}$  from the TE wave emerging from the same field. Since the Faraday rotation effect of the magnetic substrate,  $\text{Y}_3\text{Fe}_5\text{O}_{12}$ , rotates the polarization by  $280^{\circ}/\text{cm}$ , propagation of the light through 10  $\mu\text{meters}$  will give a  $\theta$  rotation of  $.28^{\circ}$ . Using a rutile prism will lend well in detecting such a small  $\Delta\theta$ .

The experimental apparatus, as shown in Figure 41, will consist of  $\text{Y}_3\text{Fe}_5\text{O}_{12}$  substrate. The rutile prisms will be used to couple light

into and out of the YIG epilayer. This device will be in the rotating magnetic field when in close proximity of a magnetic bubble memory chip. However the sampling time of the detection should be when the magnetic field is in such a position as to minimize the TE mode while no bubble is in the detectors presence. This will result in maximum sensitivity when a bubble is detected. With this setup and using a 1 milliwatt  $1.152\ \mu\text{m}$  He-Ne laser a delta intensity of approximately  $10\ \mu\text{watts}$  will be detected, which is much better than previous results.

As discussed before, prisms were not used at first due to mechanical problems. With the added detecting capability it is hoped prism coupling will prove to be more advantageous to use.

AD-A080 390

OHIO STATE UNIV RESEARCH FOUNDATION COLUMBUS  
EPITAXIAL MAGNETIC FILM EVALUATION TECHNIQUES. (U)  
NOV 79 P E WIGEN, K J BREEDING  
OSURF-764596/710525

F/G 9/2

F33615-77-C-1002

UNCLASSIFIED

AFAL -TR-79-1145

NL

2 OF 2

AD  
A080390

END  
DATE  
FILMED  
3-80



## REFERENCES

1. D. C. Fowles and J. A. Copeland; AIP Conf. Proc., 5, p. 240 (1972).
2. C. Kooy and U. Enz; Philips Res. Repts., 15, p. 7 (1960).
3. I. Maartense, C. W. Searle and M. G. Mier; J. Appl. Phys., 49, p. 1882 (1978).
4. A. A. Thiele; J. Appl. Phys., 41, p. 1139 (1970).
5. J. C. Huber; Rev. Sci. Instr., 41, p. 882 (1970).
6. P. S. Limaye, A. A. Parker, D. G. Stroud and P. E. Wigen; J. Appl. Phys. 50 2027 (1979).
7. Report #AFAL-TR-78-67, May 1978.
8. J. M. Winter, Phys. Rev. 124, 452(1961).
9. F. C. Boutron, Comp. Rend. 252, 3955(1961).
10. A. A. Thiele, Phys. Rev. B 14, 3130(1976).
11. Equations 14-17 in 2.
12. Equations 18-21 in 2.
13. P. M. Morse and H. Feshbach, Methods of Theoretical Physics; McGraw-Hill, New York, 1953; pg. 768.
14. A. H. Morrish, Physical Principles of Magnetism; Wiley, 1965; Sec. 10.3
15. A. H. Bobeck and E. Della Torre, Magnetic Bubbles; North-Holland (1975).
16. C. Kooy and U. Enz, Philips. Res. Reports., 15, p.7 (1961).
17. A. C. Gerhardstein, Dissertation, The Ohio State University, (1977).
18. P. R. Bevington, Data Reduction and Error Analysis., McGraw-Hill, (1969).
19. R. W. Shaw, D. E. Hill, R. N. Sandfort and J. W. Moody; A.P. 44, 2346 (1973).
20. P. E. Wigen, A. A. Parker, P. S. Limaye, and S. C. Hart; Bull. Am. Phys. Soc., 23, p. 65 (1978).
21. Reference Data for Radio Engineers, 6th ed. H. W. Sams & Co., Indianapolis, pp. 24, 27-24, 28.
22. J. C. Slonczewski; Intern. J. Magnetism 2, 85 (1972)

23. Dudani, S. A., K. J. Breeding, and R. B. McGhee, "Aircraft Identification by Moment Invariants," IEEE Trans. on Computers, Vol. C-26, No. 1, January, 1977.
24. Kaufman, G. J. and K. J. Breeding, "The Automatic Recognition of Human Faces from Profile Silhouettes," IEEE Trans. on Systems, Man, and Cybernetics, Vol. SMC-6, No. 2, February, 1976.
25. Goldstein, R. J., L. D. Harman, and A. B. Lesk, "Identification of Human Faces," Proc. of IEEE, Vol. 59, pp. 748-760, May, 1971.
26. Sklansky, J., Ed., Pattern Recognition Introduction and Foundations, Dowden, Hutchinson, & Ross, Inc., Stroudsburg, PA, 1973.
27. Bobeck, A. H. and H. E. D., Scovill, "Magnetic Bubbles," Scientific American, pp. 78-90, June, 1971.
28. Chen, T., et al., "High Capacity Solid State Memory Research," Interim Scientific Report, Air Force Avionics Laboratory, Wright Patterson Air Force Base, Ohio November, 1976.
29. Magnetic Bubble Memories and System Interface Circuits, Texas Instruments Inc., Dallas, Texas, February, 1977.
30. Uhr, L., Ed. Pattern Recognition, John Wiley & Sons, New York, 1966.
31. Amoss, J. O. and K. J. Breeding, "A Pattern Description Language-PADEL," Pattern Recognition, Vol. 4, pp. 19-36, January, 1971.
32. Shaw, A. C., "A Formal Picture Description Scheme as a Basis for Picture Processing Systems," Information and Control, No. 14 pp. 9-52, January, 1969.
33. Chen, C. H., Statistical Pattern Recognition, Hayden Book Co. Inc., Rochelle Park, NJ, 1973.
34. Meisel, W., Computer-Oriented Approaches to Pattern Recognition, Academic Press, NY, 1972.
35. Fu, K. S., Syntactic Methods in Pattern Recognition, Academic Press, NY, 1974.
36. Horwitz, L. P. and G. L. Shelton, "Pattern Recognition Using Autocorrelation," Proc. IRE, Vol. 49, pp. 175-185, June, 1961.
37. Carl, J. W., and C. F. Hill, "The Application of Filtered Transforms to General Classification Problems," IEEE Trans. on Computers, Vol. C-21, pp. 785-793, July, 1972.
38. Fu, J. K., "Visual Pattern Recognition by Moment Invariants," IRE Trans. on Inform. Theory, Vol. 11-8, pp. 179-187, February, 1962.

39. Production and Inspection Equipment for the Electronics Industry,  
Product Catalog, E. Leitz, Inc., Rockleigh, NJ.
40. Jagadeesh, J. M., and K. J. Breeding, "A Real Time Video Processor  
for Scene Segmentation on the Basis of Color Information,"  
Proc. of JACC, July, 1976, pp. 717-726.
41. Jagadeesh, J. M., A Real Time Image Processing System Using a  
Color Television Camera, Ph.D. dissertation, The Ohio State  
University, Columbus, OH, 1974.
42. Robinson, C. S., A Binary Image Array Processor: Hardware  
Design and Language Development, Ph.D. dissertation, The Ohio  
State University, Columbus, OH, 1977.

## APPENDIX A

### Helmholtz Coils

The drive coils used in the M-H looper are of the Helmholtz design. Helmholtz coils consist of two coils arranged such that the distance between the coil planes is equal to the mean radius of the coils. In such an arrangement, the field in the central portion of the median plane is fairly homogeneous.

The components of the field between the coils are given by<sup>A1</sup>:

$$H_z = \frac{2nI}{R} \left[ 0.44959 \left( 1 - \frac{b^2}{60R^2} \right) + 0.0035967 \left( \frac{31b^2 - 36a^2}{R^2} \right) \frac{r^2}{R^2} (3 \cos^2 \theta - 1) - 0.06474 \frac{r^4}{R^4} (35 \cos^4 \theta - 30 \cos^2 \theta + 3) \right]$$

and

$$H_x = \frac{2nI}{10R} \sin \theta \cos \theta \left[ -.0035967 \left( \frac{31b^2 - 36a^2}{R^2} \right) \frac{r^2}{R^2} + .06474 \frac{r^4}{R^4} (28 \cos^2 \theta - 12) \right]. \quad (A1)$$

The coordinate axis,  $r$ ,  $\theta$ , and  $a$  and  $b$  are defined in Figure A1.  $I$  is in amps,  $n$  is the number of turns in each coil and  $R$ ,  $a$ ,  $b$  and  $r$  are in cm. The equation assumes that the current is distributed uniformly over the crosssection  $a$ ,  $b$ .

In the median plane between the coil,  $\theta = \pi/2$ . In this case;

$$H_x = 0$$

and

$$H_z = \frac{2nI}{R} \left[ .44959 \left( 1 - \frac{b^2}{60R^2} \right) - .0035967 \left( \frac{31b^2 - 36a^2}{R^2} \right) \frac{r^2}{R^2} - 3(.06474) \frac{r^4}{R^4} \right] \quad (A2)$$

Figures A2 and A3 are a listing and typical output of a program (for a H-P 9820 calculator) to plot the magnitude of the field in the median plane. In figure A3, the coordinate  $r$  represents the distance

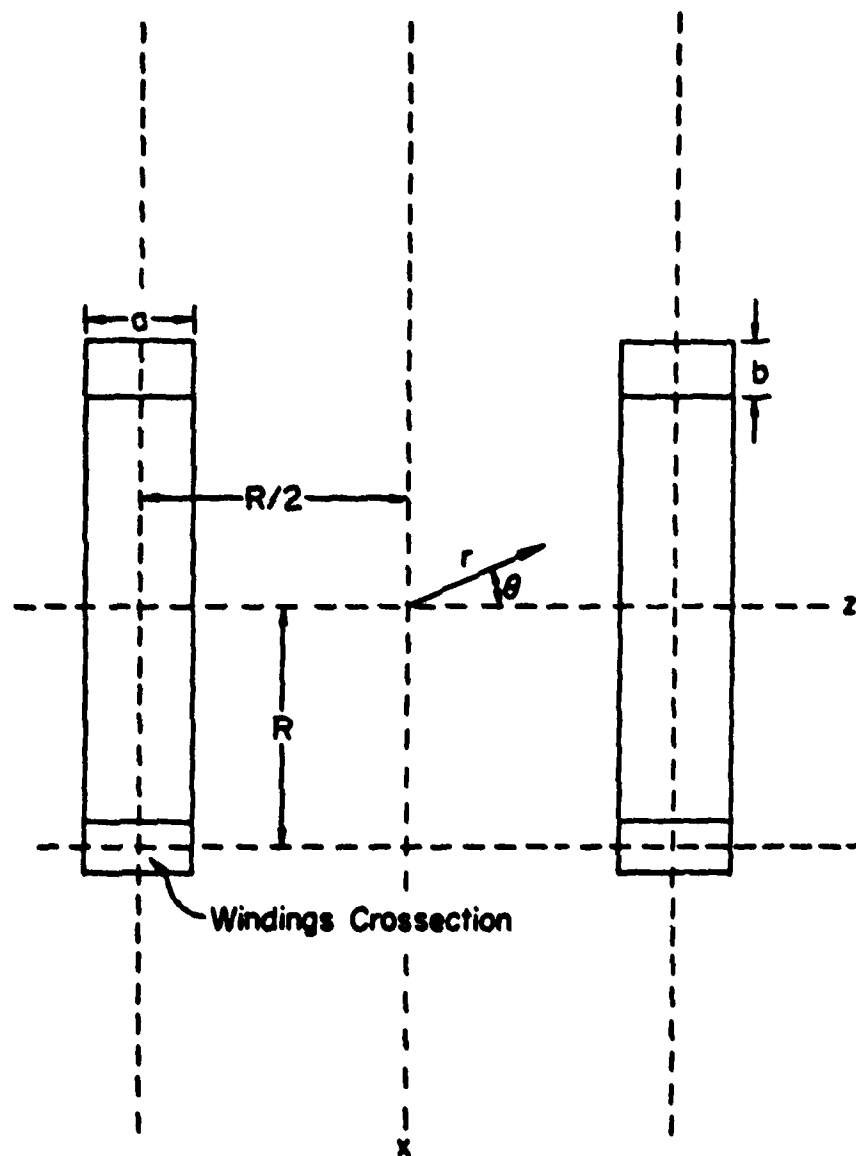


Figure A-1. Geometry of drive coils constructed for the M-H loop.

```

01
PRT "H IN MEDIAN
1PRT "PLANE SET
. TWO 1PRT "HELM
. COILS."
11
PRT "H IN GAUSS"
1PRT "R IN CM."
SPC 2H
21
ENT "COIL PA. IC
M".R0."TURNS EA
. RPH
31
ENT "A".A."B".B+
41
ENT "CURRENT IAH
PSI".PSH
51
PRT "COIL PA. = (
CH11PRT R01SPC
11PRT "TURNS EA.
"TH
61
PRT R11SPC 11
PRT "A = (CM)"
PRT R11SPC 11
71
PRT "B = (CM)"
PRT R11SPC 11PRT
"1 = (AMPS)"1PRT
R51SPC 2H
81
.44959(1-B12-60R
0121-R2H
91
.0035967(1.31812
-36R12)/R0141-R3
1
101
30.06474-R014-R4
1
111
0-N112R1P1/R01(R
2-R3-R12-R4X14)-
R6H
121
PRT "HMAX = (OE.)
11PRT R11SPC 11
PRT "R = 1PRT "-3
TO +3 CM."1SPC
2H
131
COL -3.3+0.R6+.2
R6H
141
ENT "ANES"11=Y.2
=NO1".R7H
151
IF R711GTO +2H
161
RNE 10R0+.1-R6/2
01H
171
-3+XH
181
12R1P5-R01(R2-R3
N12-R4X141-YH
191
PLT N-VIN+6-100-
XH
201
IF R131GTO -2H
211
PEN 10+XH
221
12R1P5-R01(R2-R3
N12-R4X141-YH
231
IF Y.R61.991JMP
2H
241
N+3-500-N1GTO -2
1
251
PRT "H/HMAX1.99"
1PRT "AT P = (CM)
11PRT X1SPC 10H
261
STP 1
R509
H IN MEDIAN
PLANE SET. TWO
HELM. COILS.
H IN GAUSS
R IN CM.
COIL PA. = (CM)
6.000000000E 00
TURNS EA. =
3.000000000E 02
A = (CM)
2.540000000E 00
B = (CM)
3.810000000E 00
I = (AMPS)
2.000000000E 01
HMAX = (OE.)
8.931371357E 02
R =
-3 TO +3 CM.
H/HMAX1.99
AT P = (CM)
2.926000000E 00

```

Figure A-2. Program for HP 9820 calculator used to calculate the magnetic field of the M-H looper drive coils. At the right is a typical printout.

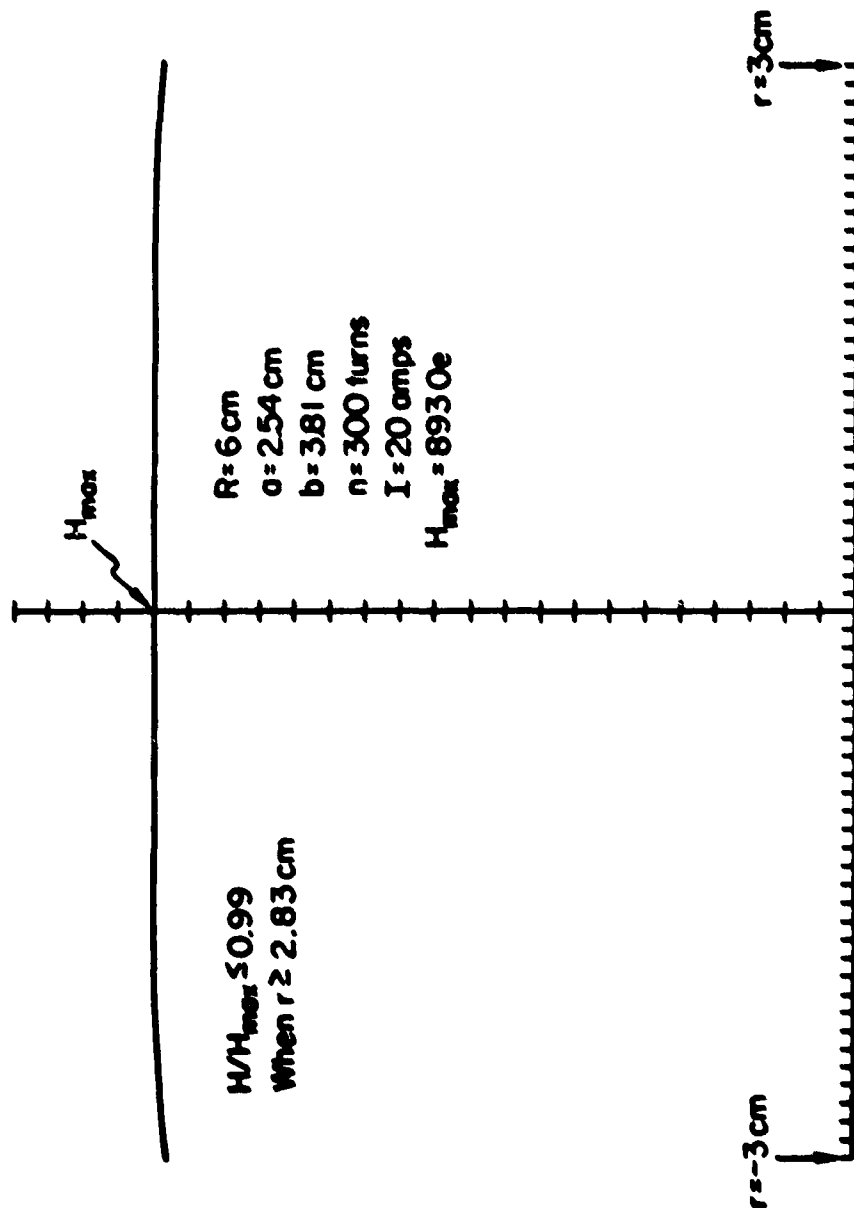


Figure A-3. A plot of the magnetic field in the median plane.

from the central point in the median plane.  $H_{\max}$  is the value of the field at the center. The program calculated that for these dimensions,  $H/H_{\max} = .99$  when  $r = 2.83$  cm. Theoretically the field should be homogeneous to 1% over a 2 inch diameter circle. The parameters used in this calculation were those used for the final coils.



## APPENDIX B

### Signal Processing Program for the M-H Looper

The computer program (for use with a HP 9825A calculator) used for signal processing on the M-H looper is listed below.

```
0: rad;fxd 3
1: dim A$ [3], B$ [3], X [500], Y [500], Z [500], T [500], Y [500]
2: time 1000
3: on err "PLOTTER"
4: rds (705) → T
5: on err "DMV"
6: rds (725) → Z
7: time 0
8: wrt 705, "IN"
9: wrt 725, "N1SR2T2F1"
10: dsp "COMMAND ?"; beep;stp
11: "PLOTTER": dsp "PLOTTER DOWN"; stp; gto 3
12: "DVM": dsp "DYM DOWN"; stp; gto 5
13: "A": 0 → A → M → F → S → P → G; ent "AVER AGING?:", A$
14: ent "FREQUENCY?", F
15: ent "SINGLE SWEEP?", B$
16: if B$ = "yes"; 1 → M
17: ina X, Y, Z, Y, T
18: for I = 1 to 500
19: 1/(500*F) → T[I]
20: next I
21: for I = 1 to 500
22: fmt "D", f.7, "S"; wrt 725
23: red 725, Y[I]; dsp I; next I
24: if A$ = "no"; gto 32
25: for J = 1 to 19
26: dsp J
```

```

27: for I = 1 to 500
28: fmt "D", f.7, "S"; wrt 725
29: 0 → G; red 725, G; Y[I]; + G → Y[I]; next I
30: next J
31: smpy .05*Y → Y
32: if M = 1; gto 36
33: ara Y → Z; 1 → M
34: beep; dsp "INSERT SAMPLE"; stp
35: gto 21
36: beep; ent "CURRENT AMPLITUDE (Amps)?", A; A*24, 59 → A; ina X
37: for I = 1 to 500
38: Acos (2πFT[I]) → X[I]
39: next I
40: gto 10
41: "D": ina V; 0 → S; 0 → P; for I = 1 to 500
42: Y[I] + S → S; Z[I] + P → P; S - P → V[I]
43: next I
44: min (V[*]) → C; max (V[*]) → E
45: scl -A, A, C, E; pen# 3
46: for I = 1 to 500
47: plt X[I], V[I]; next I
48: pen
49: gto 10
50: "G": scl -A, A, C, E; pen# 4
51: xax 0, A/5, -A, A, 5
52: yax 0, -C/10, C, E, 5; pen
53: gto 10
54: "C": ina V; ara Y - Z → V
55: for I = 11 to 239
56: V[I]/abs(sin(2πFT[I])) → V[I]; next I
57: for I = 261 to 489
58: V[I]/abs(sin(2πFT[I])) → V[I]; next I

```

```
59: for I = 490 to 500
60: 0 → V[I]; next I
61: for I = 1 to 10
62: 0 → V[I]; next I
63: for I = 240 to 260
64: 0 → V[I]; next I
65: min(V[*]) → C; max(V[*]) → E
66: scl -A, A, C, E; pen# 3
67: for I = 1 to 500
68: plt X[I] , V[I]; next I
69: pen
70: gto 10 *12610
```

# APPENDIX C

Program to calculate stripe period as a function of the bias field.

```

0 : rad; efg 14; enp "# of points". U; dim A[U, 2]; flt
1 : enp "Ku". H. "4 $\pi$ M". G. "P0". P. "Thick". T
2 : 8 $\pi$ H/G-H; 1+G/H-r1; f r1-r7; 0-K
3 : P/T-r7-P; P-X; 0-Q; geb "EVAL"
4 : -Y-K; prt "1/h="; K; epo
5 : .9/U-Q; P-A; 1-J
6 : "STP3"; 30A-B; P/30-D; 1e-9-E; 20-M
7 : prt "M/Ms="; Q; geb "ROOTS"
8 : 0-Q; for N=1 to 100
9 : sin(N $\pi$ (1+Q))-r2; exp(N $\pi$ /X)-r3
10: r3-1/r3-r4; r3+1/r3-r5; r4+r7-r5-r6
11: Y+(X-r2-r4/NN-r6-r8)-Y; next N
12: "SER": sin(N $\pi$ (1+Q))-r2; exp(N $\pi$ /X)-r3
13: r3-1/r3-r4; r3+1/r3-r5; r4+r7-r5-r6
14: Y+(X-r2-r4/NN-r6-r8)-Y
15: if abs(r8)>abs(Y) 1e-9; N+1-N; gto "SER"
16: (2r7Y/ $\pi$  $\pi$ +Q)*G-A[J, 1]; X-r7-A[J, 2]; prt "H/4 $\pi$ Ms="; A[J, 1]; epo 3; J+1-J
17: if (Q+.9/U-Q)<=.9; X-A; gto "STP3"
18: dep "Plotter on ?"; stp
19: sol 0, A[U, 1], 0, 1/P; pen# 1; xax 0, A[U, 1]/U; yax 0, .05; 1-Q; pen# 2
20: plt A[Q, 1], 1/A[Q, 2]; pens if (Q+1-Q)<=U; jmp 0
21: enp "Store inFile#". W; rof W, A[*]
22: end
23: "ROOTS": cfg 2; if A>B; efg 2; dep "ILLEGAL BOUNDS"; stp
24: A-X; geb "EVAL"
25: Y-F
26: if (A+D-A)>B; dep "No Root Found"; stp
27: A-X; geb "EVAL"
28: if (FY-Z)>0; gto -3
29: if Z<0; gto +3
30: if F=0; A-D-X; F-Y
31: A+D-A; 1e-12-S; gto +9
32: A-D-L; A-R; 0-C
33: (L+R)/2-X; geb "EVAL"
34: if (C+1-C)>M; gto +5
35: if abs(Y)<E; 0-Z; gto +2
36: if (FY-Z)>0; X-L; gto -3

```

```

37: if Z=0; R-L-S; gto +3
38: X-R; gto -5
39: R-L-S
40: (R+L)/2-X; prt "P/h="; Xr7; apo ; prt "ACCURATE TO"; S; apo ; ret
41: "EVAL"; 0-Y
42: for N=1 to 20
43: sin(Nπ(1+Q)/2)→r2; exp(Nπ/X)→r3
44: r3-1/r3→r4; r3+1/r3→r5; r4+r7r5→r6
45: Y+(r2r2(Nπr7/r6-Xr4)/NNNr6→r8)→Y; next N
46: "SUM"; sin(Nπ(1+Q)/2)→r2; exp(Nπ/X)→r3
47: r3-1/r3→r4; r3+1/r3→r5; r4+r7r5→r6
48: Y+(r2r2(Nπr7/r6-Xr4)/NNNr6→r8)→Y
49: if abs(r8)>abs(Y)1e-9; N+1→N; gto "SUM"
50: K+2r1XY/πππ→Y; ret

```

# APPENDIX D

Curve fitting program for FMR data.

```

0:  ent "Number of data pairs",N,"Number of parameters",M
1:  dim A[M],B[N],C[M],D[M],F[N],G[M,M],H[M],K[N]
2:  dim I[M],J[M,M],L[N],S[N],W[N],X[N],Y[N]
3:  dim A$(3)
4:  ent "Using uncertainties?",A$
5:  if A$="yes";efg 1
6:  prt "X1","Y1";if flg1;prt "Sigma 1"
7:  epo
8:  for I=1 to N
9:  ent "X1",X[I],"Y1",Y[I]
10: if flg1;ent "Sigma 1",S[I]
11: prt X[I],Y[I];if flg1;prt S[I]
12: epo
13: next I
14: epo
15: prt "Initial parameters";epo
16: for I=1 to M;ent "Parameter",A[I];prt A[I];next I
17: epo ;empy .01A=0
18: .001=F;oll 'Curfit'
19: C=A;prt A
20: "Loopetart";oll 'Curfit'
21: if (C-A)/A<=.01;gto "Done"
22: C=A;prt A
23: gto "Loopetart"
24: "Done";
25: prt C;epo
26: prt "Parameter","Sigma";epo
27: for I=1 to M;prt A[I],C[I];epo ;next I
28: prt "fit values";epo
29: for I=1 to N;prt F[I];next I
30: epo 3
31: end
32: "Curfit";
33: N=M-P; if P<=0; B=C;ret
34: ina W1,H,G,L1
35: if flg1;ara S=S-W;ara L/W-W
36: for I=1 to N

```

```

37: 011 'Fderiv'
38: for J=1 to M
39: H[J]+W[I]*(Y[I]..'Funotn'(I))*I[J]-H[J]
40: for K=1 to J
41: G[J,K]+W[I]*I[J]*I[K]-G[J,K]
42: next K
43: next J
44: next I
45: for J=1 to M; for K=1 to J; G[J,K]-G[K,J]; next K; next J
46: for I=1 to N
47: 'Funotn'(I)-F[I]; next I
48: 'Fohieq'-D
49: "71"; for J=1 to M
50: for K=1 to M
51: G[J,K]/f(G[J,J]G[K,K])-J[J,K]
52: next K
53: 1+F-J[J,J]
54: next J
55: inv J-J
56: for J=1 to M
57: A[J]-B[J]
58: for K=1 to M
59: B[J]+H[K]*J[J,K]/f(G[J,J]G[K,K])-B[J]
60: next K
61: next J
62: for I=1 to N
63: 'Funotn'(I)-F[I]; next I
64: 'Fohieq'-C
65: if D<C; 10F-F; goto "71"
66: for J=1 to M
67: B[J]-A[J]
68: f(J[J,J]/G[J,J])-C[J]
69: next J
70: .1F-F
71: ret
72: "Fderiv";
73: for J=1 to M

```

```

74: A[J]→X; D[J]→Z; X+Z→A[J]
75: 'Funotn' (I)→Y
76: X→Z→A[J]
77: (Y-'Funotn' (I))/2Z→I [J]
78: X→A[J]
79: next J
80: ret
81: "Fohieq":
82: B→C
83: for I=1 to N
84: C+W[I]*(Y[I]-F[I])↑2→C
85: next I
86: ret C/P
87: end
88: "Funotn":
89: B←G←B; efg 2; X[p1]→0
90: "TWO"; Y[I]sin(0-B)+.5A[2](sin(2B)→r1)→E
91: A[1](1/24*r1(1+7(cos(2B)→r2))-f2/6*sin(B)↑2(1+2r2))+E→E
92: if abs(E)<1e-9; goto "OUT"
93: if EG<0; goto "SIX"
94: B←L; E←G; B+0/10→B→R; goto "TWO"; if B>90; dep "0"; 0→B; goto "OUT"
95: "SIX"; (L+R)/2→B
96: Y[I]sin(0-B)+.5A[2](sin(2B)→r1)→E
97: A[1](1/24*r1(1+7(cos(2B)→r2))-f2/6*sin(B)↑2(1+2r2))+E→E
98: if abs(E)<1e-9; goto "OUT"
99: if EG<0; B→R; goto "SIX"; if R-L<.001; (R+L)/2→B; goto "OUT"
100: B←L; E←G; goto "SIX"; if R-L<.001; (R+L)/2→B; goto "OUT"
101: "OUT"; sin(B)↑2→p2; 0→B→K[p1]
102: sin(2B)→p3
103: 1-p2→p4
104: p4-p2→p5
105: cos(4B)→p6
106: A[1](3/16+35p6/48+5p5/12+5f2p3p2/3)→p7
107: A[1]((3-7p6+4p5)/16+f2p3(5p2/3-1))→p6

```



108: .5(A[2] (p4+p5)+p7+f ((A[2] p2+p6) ↑2+4A[3]A[3]))~p8

109: p8/000 (0-B)~p8; ret p8

110: end